SMALL ANGLE NEUTRON SCATTERING AT 4.3 MeV FROM HEAVY ELEMENTS

by

ROBERT CASSIN McFADDEN

B.Sc., St. Francis College, 1964

M.Sc., Southern Illinois University, 1966

A THESIS SUBMITTED IN PARTIAL FULFILMENT OF

THE REQUIREMENTS FOR THE DEGREE OF

DOCTOR OF PHILOSOPHY

in the Department

of

Physics

We accept this thesis as conforming to the

required standard

THE UNIVERSITY OF BRITISH COLUMBIA

July, 1974

In presenting this thesis in partial fulfilment of the requirements for an advanced degree at the University of British Columbia, I agree that the Library shall make it freely available for reference and study. I further agree that permission for extensive copying of this thesis for scholarly purposes may be granted by the Head of my Department or by his representatives. It is understood that copying or publication of this thesis for financial gain shall not be allowed without my written permission.

Department of Physics

The University of British Columbia
Vancouver 8, Canada

Date Oct 9, 1974

Abstract

The associated particle technique was employed to produce a collimated beam of 4.3 MeV neutrons from the reaction $D(d,n)^3He$. A rotating target assembly permitted the use of thin deuterated polyethylene deuterium targets. The use of a position sensitive detector in the associated particle technique was demonstrated. Data was accumulated by an on-line computer system.

The differential scattering cross section for 4.3 MeV neutrons was measured for scattering samples of uranium, bismuth, and lead over the angular range of 5^o to 15^o. The data were corrected for the effects of finite angular resolution, neutron multiple scattering, air scattering, and neutron inelortic scattering.

The experimental scattering cross sections were in agreement with those calculated on the basis of a nuclear optical model interaction plus an electromagnetic Schwinger interaction. No evidence was found to substantiate anamalous cross sections at small angles.

Give up learning, and put an end to your troubles.

Is there a difference between yes and no?
Is there a difference between good and evil?
Must I fear what others fear? What nonsense!
Other people are contented, enjoying the sacrificial feast of the ox.
In spring some go to the park, and climb the terrace,
But I alone am drifting, not knowing where I am.
Like a newborn babe before it learns to smile,
I am alone, without a place to go.

Others have more than they need, but I alone have nothing.
I am a fool. O, yes! I am confused.
Other men are clear and bright,
But I alone am dim and weak.
Other men are sharp and clever,
But I alone am dull and stupid.
Oh, I drift like the waves of the sea,
Without direction, like the restless wind.

Everybody else is busy,
But I alone am aimless and depressed.
I am different.
I am nourished by the great mother.

Lao Tsu , Tao Te Ching

as translated by Gia-fu Feng

Table of Contents

List of Figures

List of Tables

Publications

R. McFadden, P.W. Martin, and B.L. White, "An Associated Particle Time of Flight System Using a Position Sensitive Detector", Nuclear Instruments and Methods 92 (1971) 563.

R. McFadden and P.W. Martin, "A Rotating Target Assembly for Thin Targets", Nuclear Instruments and Methods 113 (1973) 601.

P.W. Martin, R. McFadden, and B.L. White, "Small Angle Scattering of 4.3 MeV Neutrons from U, Bi, and Pb", Canadian Journal of Physics 51 (1973) 2197.

Acknowledgements

I want to express my appreciation for my association with Peter Martin.

Also, I wish to mention here Bruce White, George Griffiths, and Eric Vogt. I have enjoyed my time spent with my friends Rich Helmer, Johnnie Heggie, Jack Beveridge, Peter Bosman, and Søren Lemche.

My appreciation is extended to my parents John and Rebecca McFadden. Finally, Elinore King who has shared my pleasures and pains.

CHAPTER 1

Introduction

1.1. General Introduction

The importance attached to the study of the scattering of neutrons by nuclei as a means of gathering information from the world of the nucleus is evidenced by the large number of experimental and theoretical investigations devoted to the subject. The analysis of neutron scattering data sheds light upon three fundamental aspects of nuclear physics. These are:

i) properties of the nucleus

ii) nucleon-nucleus interaction

iii) properties of the neutron .

At incident neutron energies in the MeV range the most likely process is that of elastic scattering. Here the neutron transfers no energy to the internal structure of the target nucleus and, apart from the recoil energy of the nucleus, has the same energy after the interaction as before. The momentum and spin state of the neutron however are in general changed by the collision. It is from an analysis of these effects that inferences about the nature of the interaction and of the neutron and nucleus can be made.

The work described in this thesis was undertaken to elucidate certain problems associated with the specific area of neutron elastic scattering at small angles. In order to delineate these problems a

review is given of the optical model for neutron scattering, with the further inclusion of those terms in the Hamiltonian important to the description of small angle processes. A resume of previous experimental work then follows from which will be seen to emerge the motivation for further measurements.

The impetus for the present work was provided by the conflicting nature of the available data from previous small angle scattering measurements, a feature manifestly demonstrated by the experimental points of figure 1-1, after (Vo 69). Neutron scattering experiments are notoriously difficult, usually subject to high background levels and, particularly in the small angle regime, requiring careful corrections for such effects as geometry, multiple scattering, and air scattering. Furthermore, in the region around 4 MeV incident neutron energy no previous measurements at angles less than 10^{o} (Tr 67) had been made incorporating fast timing techniques, reliance having been placed on massive shielding and mechanical collimation. An independent investigation, therefore, using neutron time-of-flight methods seemed to offer desirable advantages. To achieve this end, the $D(d,n)^{3}He$ reaction was chosen as the neutron source. By detecting in coincidence the ^{3}He particles emitted in this reaction, it was possible to define an associated beam of outgoing neutrons of energy 4.3 MeV. Neutrons scattered out of this beam by a suitably interposed scatterer were detected by their time-of-flight to a detector placed at an appropriate angle to the beam.

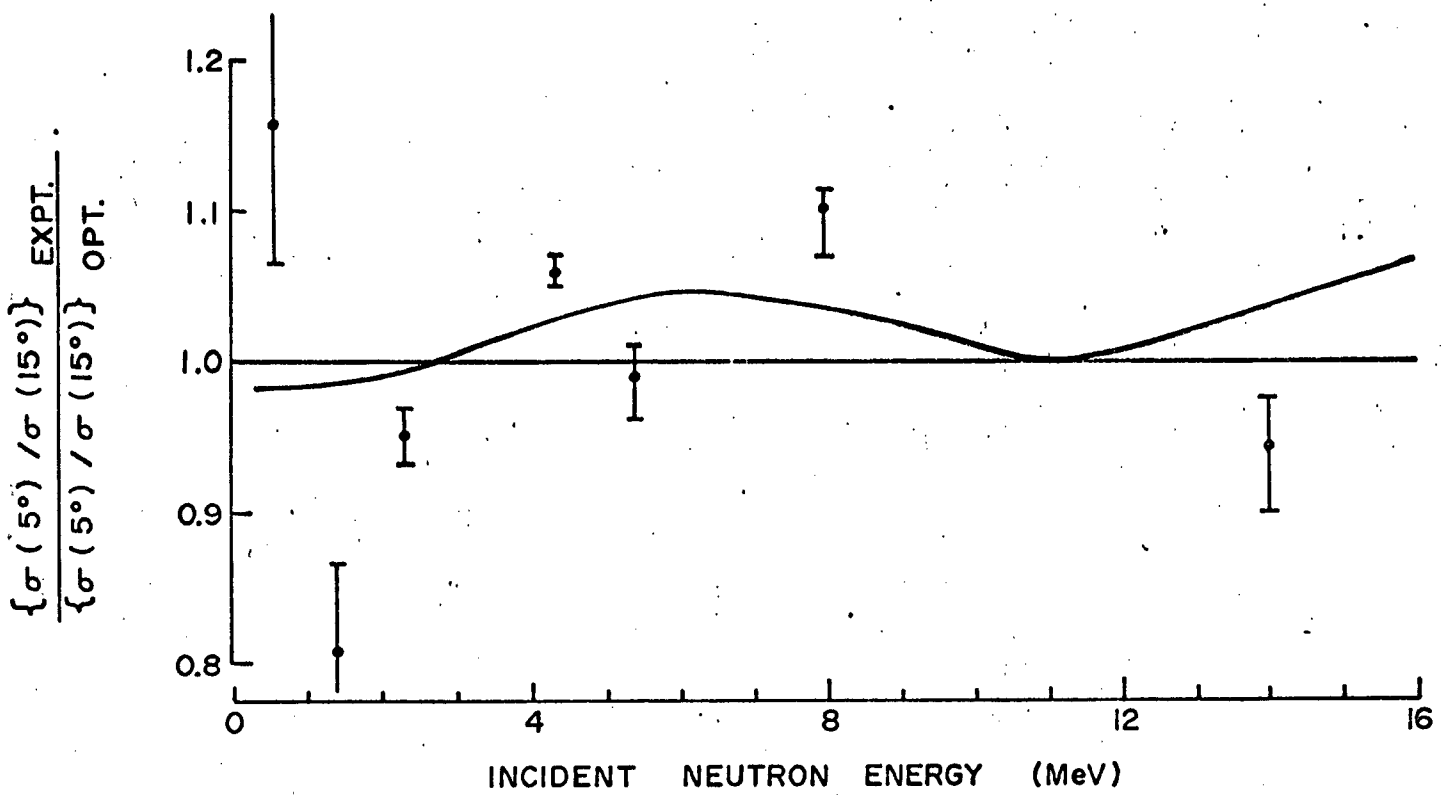

Figure 1-1 Comparison of Optical Model and Experimental Cross Sections. Solid Curve From Vogt (Vo 69).

1.2.1 The Optical Model of Scattering

In 1952 Barschall (Ba 52) examined the current experimental data on total neutron cross sections (Mi 52) and plotted them as a function of incident neutron energy and target nucleus atomic weight. The cross sections changed very little for neighboring atomic weights but changed markedly over the range of atomic weights surveyed, Aw = 60 to Aw = 240 (see also (Fe 54)). Broad maxima and minima occured whose position varied only slowly with atomic weight. This same behavior was later shown to be exhibited by neutron angular distribution data (Wa 54) and neutron polarization data (Ro 61). These same remarks apply to data for other incident particles as well.

Regularities of this nature can be interpreted as evidence that the neutron-nucleus interaction may be accounted for by a model which takes into account only the gross properties of the target nucleus such as the atomic weight and the distribution of nuclear matter. The detailed structure of the nucleus or neutron does not enter into this model, at least to first order.

LeLevier and Saxon (Le 52) first used a complex potential well, an "optical model", and solved Schrodingers equation to describe data on 18 MeV proton scattering from aluminum which showed a diffraction pattern angular distribution for the elastic scattering. Later Feshbach (Fe 54) used an interaction of the form

$$V(r) = V_o(r)\ (1 + i\delta) \quad ,$$

and solved Schrodingers equation to account for the neutron data of

Barschall and Miller. The potential employed a simple square well radial dependence with a depth of 42. MeV and radius 1.45 $A^{1/3}$ fm. The imaginary term used was $\delta = 0.03$.

Later developments of the optical model with more realistic potentials (as described below in 1.2.2.) have been able to reproduce scattering results over the energy range of approximately 1 MeV to 300 MeV. On the lower side of this range isolated resonances of the compound nucleus dominate the scattering. These resonances depend upon the specific nuclear structure of the states involved and so cannot then be described by the average two body potential of the optical model. As the incident neutron energy increases the compound nucleus resonances become narrowly spaced and are averaged by the resolution of the experimental apparatus. The cross section then consists of shape elastic and averaged compound elastic components which vary smoothly. Compound elastic effects finally become small at about 5 MeV to 10 MeV for heavy nucleii. At high energy relativistic effects enter the calculation as does the necessity of including large numbers of partial waves. Computational difficulties then begin to limit the usefulness of the optical model until at about 500 MeV approximate solutions become necessary.

Apart from the phenomenological basis of the optical model potential, some theoretical justification does exist. At high energies of a few hundreds of MeV the form of the optical model potential can be derived from the two body nucleon-nucleon interactions (see for example (Ke 59)). Here the wave length of the neutron is small with respect to the separation of target nucleons and correlation effects are small. An impulse approximation is possible because of the large incident neutron energy compared to the

binding energy of the target nucleons. In this case the incident neutrons are multiply scattered by the nucleons in the target and the scattering amplitude can be obtained from a sum of the nucleon-nucleon amplitudes over the nucleus. At lower energy the derivation becomes difficult but results have been obtained from Brueckner calculations. These theoretical studies give the forms of the optical model potential terms discussed below.

1.2.2. Terms of the Optical Model Potential

The real potential acting on an incident neutron is constant inside the nucleus as the neutron sees only the neighboring nucleons surrounding it. At the surface the rapid exponential fall off with distance characteristic of nuclear forces may be expected. The Saxon-Woods potential form gives these features with a radial dependence

$$(1\text{-}1) \qquad f(r) = \frac{1}{1 + \exp((r-R)/a)} \quad .$$

Where

$R = R_o A^{1/3}$ = nuclear radius fm.

a = surface diffuseness fm.

The imaginary potential representing the absorbtion of the incident beam by the target nucleus is surface peaked at low energies of 1 MeV to 10 MeV and a gaussian form will give this behavior with

$$(1\text{-}2) \qquad g(r) = \exp\{ - ((r-R_o A^{1/3})/b)^2 \} \quad .$$

Here

b = surface diffuseness fm.

A Saxon-Wood derivative term is possible and yields similar results. The calculated cross sections are not sensitive to these forms of the imaginary well. However at hundreds of MeV volume absorbtion does become important.

Nuclear forces are spin dependent and show polarization effects. This may be taken into account by coupling the angular momentum L with the neutron spin through the term $L\cdot\vec{\sigma}$. Here $\vec{\sigma}$ is the Pauli spin matrix. The theoretical calculations discussed above indicate a Thomas or real well derivative form

$$h(r) = (h/m_{\pi}c)^2 \left(\frac{1}{r}\frac{df(r)}{dr}\right) \quad . \tag{1-3}$$

The optical model potential now is comprised of three terms

$$V_{OM}(r) = Vf(r) + iWg(r) + V_s h(r) \; \vec{L}\cdot\vec{\sigma} \quad . \tag{1-4}$$

The constants V, W, and V_s give the well depths. Together with the well diffuseness lengths a and b and the well radius R_o they comprise the adjustable optical model parameters.

1.2.3. Electromagnetic Neutron-Nucleus Interactions

For neutrons the effect of the nuclear electric field

$$\vec{E} = Z\, e\, \vec{r} \,/\, r^3 \tag{1-5}$$

becomes important with large Z nuclei and two electromagnetic interactions are of interest. The Schwinger interaction is first order

in $\vec{E}$. Schwinger (Sc 48) considered the interaction of the neutron magnetic moment

$$\vec{M} = -\vec{\mu}_n \frac{e\,h}{2mc} \tag{1-6}$$

with the magnetic field in the frame of reference of the incident neutron

$$\vec{H} = \frac{1}{c}\,\vec{E} \times \frac{\vec{P}}{m} \tag{1-7}$$

The interaction energy is given by

$$V_{Sc} = -\,\vec{M}\cdot\vec{H} = \mu_n \frac{e\,h^2}{2\,m^2\,c^2}\,\sigma\cdot\vec{E} \times \vec{p} \tag{1-8}$$

In order to see the radial dependence recall that

$$\vec{L} = \frac{\vec{r} \times \vec{p}}{n}$$

and we have

$$V_{Sc}(r) = \mu_n \frac{Z\,e^2\,n^2}{2\,m^2\,c^2}\,\frac{\vec{L}\cdot\vec{\sigma}}{r^3} \tag{1-9}$$

From a Born approximation calculation Schwinger obtained for the scattering cross section

$$\sigma(\theta) = f_o(\theta)^2 + \frac{\varepsilon^2}{16}\cot^2\theta/2 + \frac{\varepsilon}{2}\,\vec{P}\cdot\vec{n}\ \mathrm{Im}\ f_o(\theta)\cot\theta/2 \tag{1-10}$$

where

$f_o(\theta)$ = nuclear scattering amplitude

$$\varepsilon = 2\mu_n \frac{Z\,e^2}{m\,c^2}$$

$\vec{P}$ = incident neutron polarization

$\vec{n}$ = normal to reaction plane .

The expression for the polarization is

$$(1\text{-}11) \qquad P(\theta) = \frac{2\ \mathrm{Im}\ f_o(\theta)\ \epsilon/4\cot\theta/2}{|f_o(\theta)|^2 + (\epsilon/4)^2\ \cot^2\theta/2}$$

The Schwinger scattering contribution to the cross section is significant at scattering angles less than 10^o for the high Z elements. At angles less than 2^o Schwinger scattering rises very rapidly and the polarization approaches 100%. In this region the effect may be used as a polarization analyzer (Ga 72) or as a source of polarized neutrons as Schwinger originally suggested. The only large angle effect of the electromagnetic interaction is seen in the values of the polarization at 24^o (Mo 64).

A second electromagnetic interaction, quadratic in the nuclear electric field E, arises from the possibility of inducing an electric dipole moment in the neutron. The neutron possesses internal structure (Li 61) and in particular an electric charge distribution. The presence of an external electric field distorts the charge distribution and the electric dipole moment becomes

$$(1\text{-}12) \qquad \vec{P} = \alpha\vec{E}$$

where α is the neutron polarizability. The interaction of this dipole moment with the electric field is (Bar 57)

$$(1\text{-}13) \qquad V_p = -\alpha\frac{\vec{E}\cdot\vec{E}}{2}$$

$$V_p = -\alpha\frac{Z^2e^2}{2}\ \frac{1}{r^4}\ .$$

Barashenkov has given the Born approximation for the scattering cross section as

$$(1\text{-}14) \qquad \sigma(\theta) = |f_o(\theta)|^2 + |f_s(\theta)|^2 + f_p(\theta)\ R\ f_o(\theta) + \tfrac{1}{4} f_p^2(\theta)$$

where

$$(1\text{-}15) \qquad f_s(\theta) = \tfrac{1}{4}\ (\varepsilon \cot\theta/2)$$

$$(1\text{-}16) \qquad f_p(\theta) = \frac{\alpha}{2}\ \frac{Z^2\ c^2}{R}\ K\ R\ \left(\frac{\mathrm{Sin}\ K\ R}{K^2\ R^2} + \frac{\mathrm{Cos}\ K\ R}{K\ R} + \mathrm{Sin}\ K\ R\right) ,$$

$$K = \sqrt{8Em}\ \ \mathrm{Sin}\theta/2 \quad .$$

A value of the polarizability α has been obtained from $P(\gamma,\pi^+)n$ experimental data by Breit (Br 59) as

$$\alpha = 1.2 \times 10^{-42}\ \mathrm{cm}^3 \quad .$$

Calculated neutron polarizabilities lie in the range

$$2 \times 10^{-43}\ \mathrm{cm}^3 \leq \alpha \leq 8 \times 10^{-41}\ \mathrm{cm}^3$$

(Bar 62) (Bal 57) (Th 59) (Bar 63). Estimates of the polarizability from neutron scattering data suffer from difficulties in interpreting experimental results which include the large nuclear interaction contribution. These results are discussed below. A hopeful suggestion has been forwarded that the neutron polarizability may be determined by examining the small angle scattering of slow neutrons from a high flux reactor by the standing electromagnetic wave in a very high power laser cavity (St 73). If in the future sufficiently high neutron and photon densities can be obtained, and this appears feasible, the experiment would allow an interpretation in terms of the well understood electromagnetic interaction.

A more complete description of the neutron-nucleus interaction can be now written as the sum of the nuclear optical model potential and

the electromagnetic terms. Combining equations (1-4), (1-9), and (1-13) we have

$$V(r) = V_{om}(r) + V_{Sc}(r) + V_{p}(r) \quad . \tag{1-17}$$

This is the interaction which must be considered for neutron scattering at angles less than 10^{o}.

1.3.1. Other Techniques and Measurements

Neutron angular distribution data for small angles are available from 0.57 MeV to 120. MeV. These data are marked by a number of conflicting results some of which indicate anomalous behavior on the part of the angular distributions at scattering angles below 10^{o}. This behavior takes the form of a rapid deviation of the experimental cross sections from those calculated using the optical model and known electromagnetic interactions. The behavior is not a simple function of incident neutron energy.

The following Table 1-1 summarizes the results and techniques of previous work on small angle scattering. On the left side of the table in the order of increasing energy, experimental results are listed. The theory on which the conclusions were based and the reference from which they are taken are included. For each nucleus and energy the existence of a measurement is indicated by the presence of "-", "o", or "+". These indicate that the experimental results at small angles were "less than", "in agreement with", or "greater than" theoretical predictions, respectively. This is in each case based on the angular variation of the cross section not on the absolute magnitude. In the

case of the group of nuclei, the presence of more than one "o" indicates that measurements for more than one nucleus of that group were made at that energy.

The theoretical models referred to by number are the following:

1) optical model plus Electromagnetic interaction(s)

2) $\sigma(\theta) = A \cos(\theta) - B$

3) opaque nucleus with diffraction

$\sigma(\theta) = \sigma(0^{o}) \{2J_1(kR\theta) / kR\theta\}^2$

J_1 = Bessel function

k = neutron wave number

R = nuclear radius

4) optical model plus Schwinger interaction

$\Sigma(\theta) \equiv \sigma(\theta) P(\theta) / \sigma_t$

Experimental techniques as described in the references are listed on the right of the table. The neutron beam energy spread, the neutron source, and in a few cases where applicable the timing method are indicated. The term "mono" refers to monoenergetic neutrons as obtained from a collimated reaction source. The energy dispersion of neutrons from such a source has been investigated in at least one instance (Wa 64). The neutron sources are designated in the following manner

R = reactor

Li = $^{7}Li(p,n)^{7}Be$

D = $D(d,n)^{3}He$

T = $T(d,n)^{4}He$

C = cyclotron internal target .

Timing was accomplished by pulsed beam, the associated particle technique, or the time structure of the cyclotron beam.

Inelastically scattered neutrons were corrected for and/or discriminated against. This was accomplished by either time-of-flight measurements or biased neutron detectors. The designation "n-γ disc" refers to neutron-gamma ray discrimination by pulse shape analysis. This has been widely used. Multiple scattering corrections have usually been performed, as have solid angle corrections. The later are important especially at angles less than 3^{o} where the cross section varies rapidly with angle because of Schwinger scattering. Air scattering accounts for much of the background at small angles and should be considered. See section 4.2.1. below and (Ku 68). Note that " * " designates the following:

Broad energy spectrum.

(Al 58) Peak at 1.3 MeV. Lower cut off 1.1 MeV. Upper cut off 5 MeV. "mean effective energy" = 2 MeV.

(Al 57) "effective neutron energy" = " 3-4 MeV "

Some remarks about the anomalies indicated in the table should be appended. In the data of Anikin from 0.57 MeV to 14. MeV as presented by Pery (Pe 66) (An 71) the observed scattering anomaly, of up to 13% at 5^{o}, lies in the angular range 2^{o} to 10^{o}. Alexandrov (Al 58) (Al 61) observed similar anomalous cross sections. Dukarevich (Du 63) observed anomalies only below 5^{o} of some 17% at 2^{o} for 14.2 MeV.

Drigo et. al. (Dr 73) have shown a 14% anomaly based upon one point at 2^{o} for 2.45 MeV. The deviation was attributed to the polarization

		Pu	Th	U	Bi	Pb	Au, W, Sn, In, Cd, Cu	Theory	ΔE MeV	Source	Timing	Inelastic	N-γ Disc.	Mul. Scatt.	Air Scatt.	Solid Angle	Scattering Angles (degrees)
Wa 64	0.57			0				1	Mono	Li		✓	✓	✓	✓	✓	3.6-18
An 71	0.575			+				1	0.2	R		-	-	✓	-	✓	2.5-25
Ku 68	0.6		0	0			0	1	Mono	Li		✓	✓	✓	✓	✓	1.5-15
Al 61	0.8		0	0			0	2	-	R		-	-	-	-	-	3-25
Ku 68	0.84		0	0		0	00	1	Mono	Li		✓	✓	✓	✓	✓	1.5-15
Ku 68	1.00		0	0			000	1	Mono	Li		✓	✓	✓	✓	✓	1.5-15
Ku 68	1.2		0	0			00	1	Mono	Li		✓	✓	✓	✓	✓	1.5-15
An 71	1.33			-		-	0	1	0.4	R		-	-	✓	-	✓	2.5-25
Ku 68	1.6		0	0			0	1	Mono	Li		✓	✓	✓	✓	✓	1.5-15
Al 58	2*	+		+	0	0	00	2	*	R		-	-	-	-	-	4-25
An 71	2.45			-		-	0	1	0.7	R		-	-	✓	-	✓	2.5-25
Dr 73	2.45				0	+		4	Mono	Li	Pulsed Beam	✓	✓	✓	✓	✓	2.1,3,5
Al 61	2.8		+	+			0	2	-	R		-	-	-	-	-	3-25
Al 57	3-4*			0			0	1	*	R		-	-	-	-	-	0.5-8
Go 69	4.			0	0	0	000	1	0.4	D		✓	✓	✓	✓	✓	2-21
An 71	4.5			+		+		1	1.5	R		-	-	✓	-	✓	2.5-25
An 71	5.6			0				1	1.5	R		-	-	✓	-	✓	2.5-25
An 71	8.4			+		+		1	1.5	R		-	-	✓	-	✓	2.5-25
Du 63	14.		+	+	0	0	0	3	Mono	T	Ass. Part	-	-	✓	-	-	3-20
An 71	14.			-		-		1	-	-		-	-	✓	-	✓	2.5-25
Ad 69	14.			0				1	Mono	T	Ass. Part	✓	-	-	-	-	4-20
Bo 63	18 to			0				1&3	4. to	C	Cyclo-tron	✓	-	✓	-	-	1,2-5,
Bo 63	120			0				1&3	15.	C	Bunch	✓	-	✓	-	-	4.5

Table 1-1 Previous Experimental Work.

rather than to the cross section in their expression

$$\Sigma(\theta) \equiv \sigma(\theta)\ P(\theta) / \sigma_T \quad . \tag{1-18}$$

Vogt (Vo 69) has shown the quantity

$$\{\sigma(5^o) / \sigma(15^o)\}_{expt.} \qquad \{\sigma(5^o) / \sigma(15^o)\}_{Theo.}$$

as a function of neutron energy as in figure 1-1. The experimental and theoretical cross sections, are from Anikin (Pe 66) (An 71). Gorlov (Go 70) has displayed the sign of the anomaly for the published work as of that date for low energy ($\leq$ 14 MeV).

In an early work of the Argonne group of Elwyn (El 66) an anomalous result was reported for uranium at 0.83 MeV over the angles 1.65^o to 4.6^o. This observation was not substantiated by later work of the same group of investigators (Ku 68). This points up the difficulties attending small angle scattering experiments.

1.3.2. Theoretical Interpretations

Several attempts have been made to interpret small angle data which is not successfully fit by a nuclear optical model plus a Schwinger interaction. First, several workers have adjusted the value of the polarizability to improve the agreement between a nuclear plus electromagnetic interaction calculation and the data. The most comprehensive attempt is due to Anikin who optimized the fit to data over the range 0.57 to 8.4 MeV and over the angular range 2.5^o to 23.8^o for uranium, lead, and copper. The value of $\alpha = 2 \times 10^{-40}$ cm^3 obtained

is large compared to other values discussed in section 1.2.3. The interpretation of the fit to the data seems to suffer from the significant energy spreads in the neutron beam and no consideration of possible inelastic contributions to the data. Furthermore there is difficulty isolating the small polarizability effect from possible unknown nuclear interaction effects in such a curve fitting procedure.

For example, Vogt (Vo 69) has suggested a nuclear structure effect. Consider neutrons incident on uranium. If there is significant alpha clustering in the nuclear surface then the neutron scattering can take place from a ^{234}Th core plus an alpha particle.

Now in the neutron-^{4}He system there is a broad resonance peaked at 1 MeV, the ground state and the first excited state of ^{5}He. Because of this p-wave resonance the surface alpha cluster is almost as intense a scatterer as the ^{234}Th core. The two scattering centers of the alpha particle - ^{234}Th core system act like a two slit classical optics system and produce a forward peaked interference pattern. The magnitude of this effect was calculated by making some assumptions about the number of alpha particles in the surface and their spatial distributions. The solid curve of figure 1-1 shows the estimated effect up to 16 MeV incident neutron energy.

It has also been suggested that the small angle enhancement may be associated with some property of fissionable nucleii. Gorlov (Go 70) argues against this on the basis of the oscillating behavior of the anomaly with energy. Lead also shows anomalous results.

Other electromagnetic effects, the atomic electrons (Bar 62) and electric quadrupole and magnetic dipole moments (Bar 57), are too small

to offer an explanation. Redmond has shown that a strong surface spin orbit force can affect small angle cross sections (Re 65).

1.3.3. Present Experimental Work

Tripard (Tr 67) has demonstrated the possibility of using the associated particle technique with the $D(d,n)^3He$ reaction to produce a collimated 4.5 MeV neutron beam for experiments in the angular range 10^o to 40^o. In this energy region the previous work of Alexandrov and Bondarenko (Al 57) at 3-4 MeV showed no anomalous effects for copper and lead. Similarly Gorlov et. al. (Go 69) found no effects for copper, lead, bismuth, and uranium as well as other elements at 4. MeV. However at 4.5 MeV Anikin (An 71) (Pe 66) found anomalous increases in the cross sections for lead of 5% at 5^o and for uranium of 6% at 5^o but not for copper and smaller.

The present work was undertaken to obtain scattering cross section data at small angles at 4.3 MeV for the heavy elements lead, bismuth, and uranium. In order to extend the measurements of Tripard (Tr 67) to smaller angles and to improve signal to background ratios, several developments in the associated particle technique were initiated. Fast timing offered some advantages over the other neutron beam sources previously used. A reduction of the background counts and an "electronic collimation" of the neutron beam were achieved by the coincidence operation of the neutron and recoil particle detectors. Inelastically scattered neutrons could be discriminated against on the basis of the

information contained in the time-of-flight difference between the neutron and recoil particle. The energy spread of the neutron beam, governed by the reaction kinematics and the recoil detector geometry, could be held to a low value. Finally, since the neutrons are polarized, the possibility of studying polarization phenomena was available.

Several other developments were incorporated into the experimental design. Neutron-gamma ray pulse shape discrimination was used in the neutron detector electronics to reduce the background of counts. The use of a position sensitive charged particle detector to allow the study of the angular variation of the cross sections was investigated. The following chapters cover the experiment in some detail.

CHAPTER 2

Neutron Beam

2.1.1. Reaction Kinematics

The $D(d,n)^3He$ reaction was employed as the neutron source reaction. The reaction is exoergic with Q=3.28 MeV. Within the energy range of the University of British Columbia Van de Graaff (0.6 MeV to 3 MeV) neutrons of between 1 MeV and 6 MeV may be produced with this source reaction. The neutrons are partially polarized, a local maximum in the polarization occurring at E_d=2.0 MeV where p_m=-15% for $\theta_m=49^o$ (Du 61, Bar 65). Here the sign of the polarization is fixed by the Basel convention, (Bas 61).

The $D(d,n)^3He$ reaction kinematics for E_d=2.0 MeV and the angular region centered on $\theta_m=49^o$ are shown in figure 2-1. From this diagram the ^3He particle associated with a neutron at $\theta_m=49^o$ emerges with a recoil energy of 0.953 MeV. In practice this is sufficient energy to permit the use of a silicon surface barrier detector with good timing characteristics in the associated particle technique. At recoil energies substantially below this, $E_{^3He}$ 0.5 MeV, detector and electronic noise problems raise serious difficulties in obtaining timing signals for use in time-of-flight measurements.

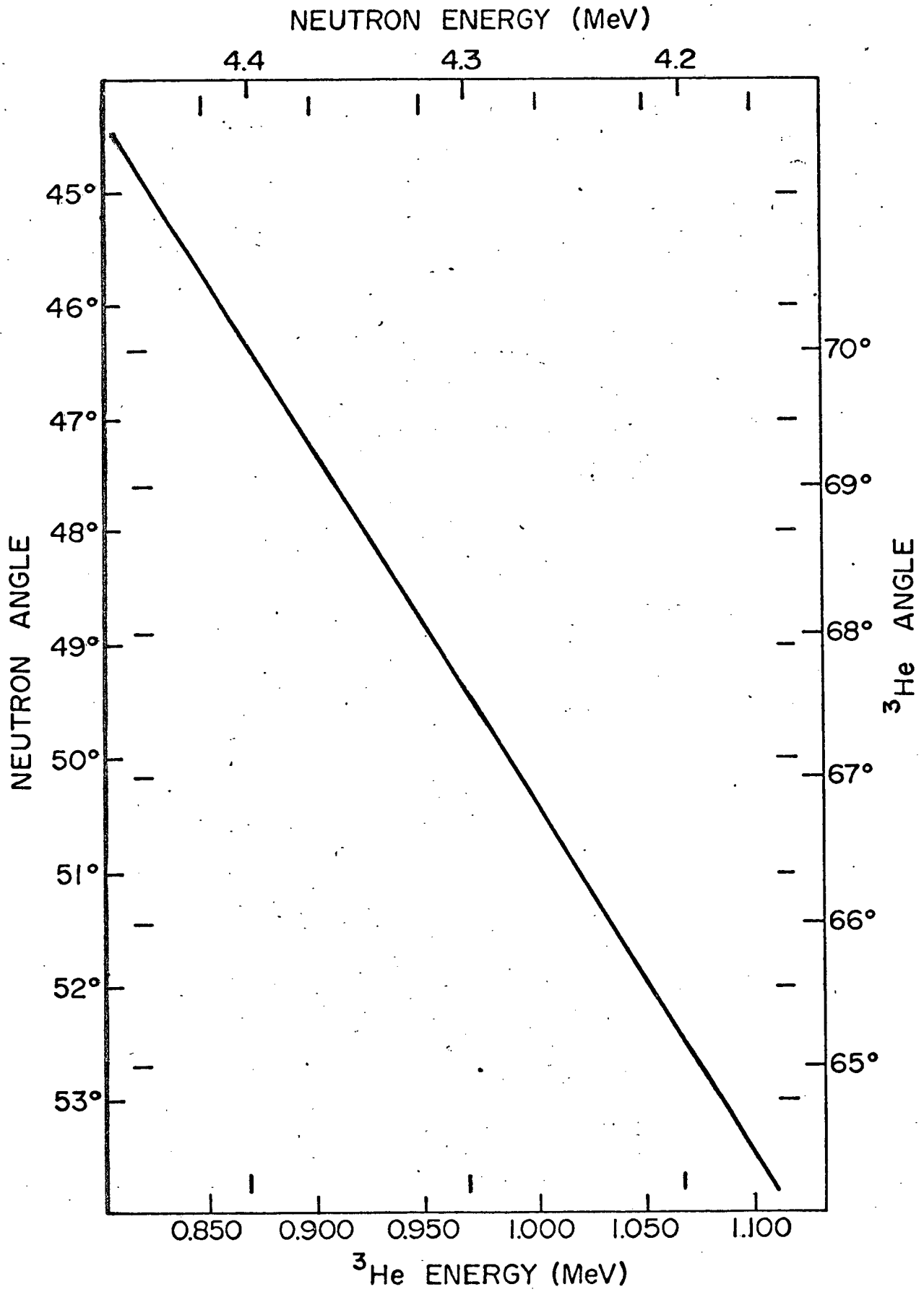

Figure 2-1 D(d,n)^{3}He Reaction Kinematics

2.1.2. Neutron Beam Characteristics

The profile of the incident deuteron beam spot and the ^3He detector collimator determine the angular acceptance of the ^3He particle detector when used with a thin deuterium target. The figures of diagram 2-2 illustrate this for the conditions of the present experiment.

The range of angles over which it is possible for ^3He particles to reach the ^3He detector is the full width at minimum intensity, with a value of 4.7^o, shown in figure 2-2a. The narrower range of angles over which ^3He particles from any part of the target may reach the ^3He detector is the full width at maximum intensity, with a value of 3.5^o, shown in figure 2-2b. The full width at half maximum intensity lies midway between these values.

For a ^3He recoil particle detector centered at the laboratory angle of 68^o the corresponding neutron beam widths may then be read off the kinematic curve of figure 2-1. A neutron beam profile constructed from this information is shown below in figure 2-12. The full width at half maximum of the horizontal neutron beam profile is expected to be 5.1^o.

Similarly, the vertical neutron beam profile may be derived. In this case, the symmetry of the kinematics under a rotation about the incident deuteron beam means that the geometry of the beam spot and the ^3He detector collimator (3.5 mm) alone determine the neutron beam profile. The vertical width is expected on this basis to be 1.1^o full width at half maximum intensity.

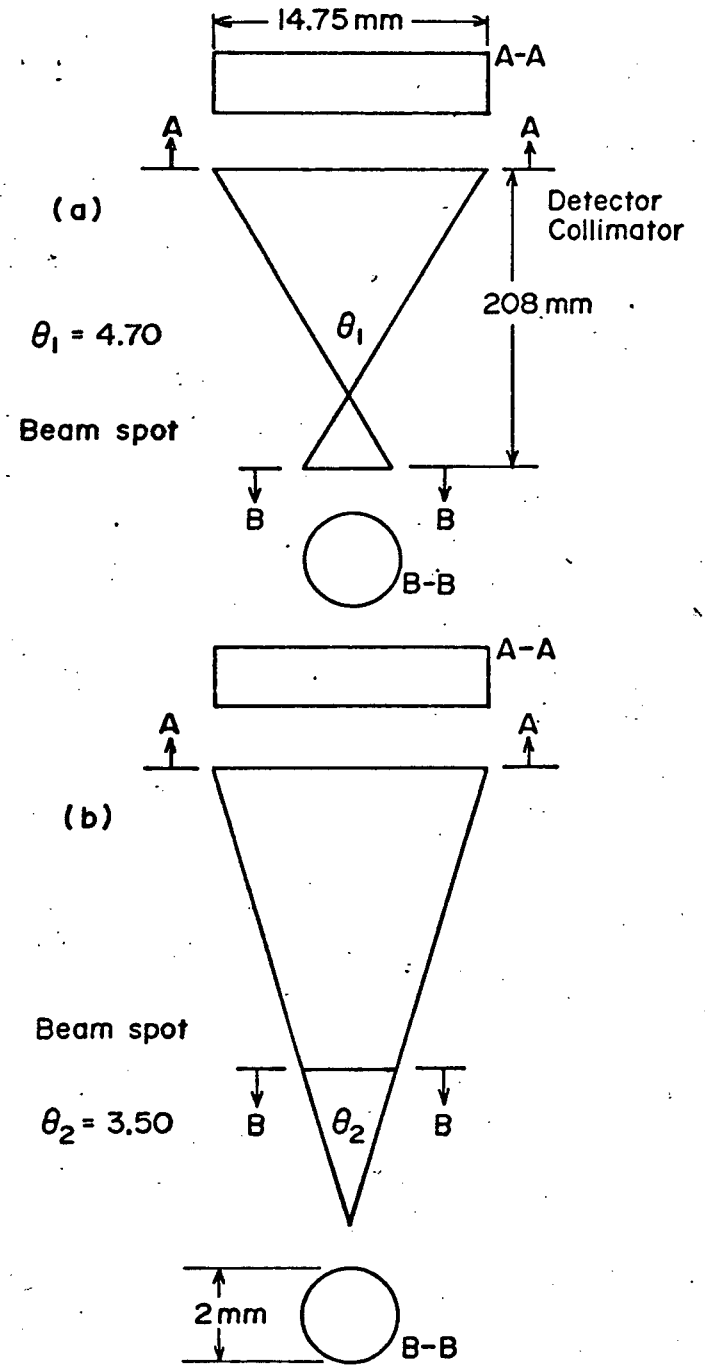

Figure 2-2 Deuteron Beam Spot and ^{3}He Detector Geometry

Finally the energies and the energy spreads may be obtained from figure 2-1, yielding the neutron beam energy E_m=4.3 MeV and the energy spread, ΔE_m=0.168 MeV. Correspondingly, we find the ^{3}He recoil energy, $E_{^3He}$=0.953 MeV with $\Delta E_{^3He}$=0.166 MeV.

2.2.1. Beam Line and Target Chamber

The incident 2 MeV deuteron beam was obtained from the University of British Columbia 3 MeV Van de Graaff accelerator, shown in figure 2-3 in horizontal view. Also shown in this figure are the deuteron beam transport system, the beam current at several points typical of experimental conditions, and shielding in the experimental area.

As evident, a large fraction of the total deuteron beam current was lost in the Van de Graaff machine and beam transport system. The remainder, approximately 10%, was eventually deposited in the beam stop. Reactions of the type (d,n), (n,n$'$,γ), (n,γ) and, within the Van de Graaff machine itself, (e,γ), constituted sources of background counts in the detectors. These counts were not time correlated between the detectors, but increased the detector "singles" count rates, thus raising the random coincidence rate and dead time losses. While it was true that the use of a time-of-flight system greatly reduced background events, the use of shielding was necessitated to reduce the singles count rates to tolerable levels.

Shielding was placed at two locations. First, a 40 cm wax - 40 cm concrete wall was constructed between the machine area and the experimental area. Second, an open-ended room of 39 cm concrete, wax,

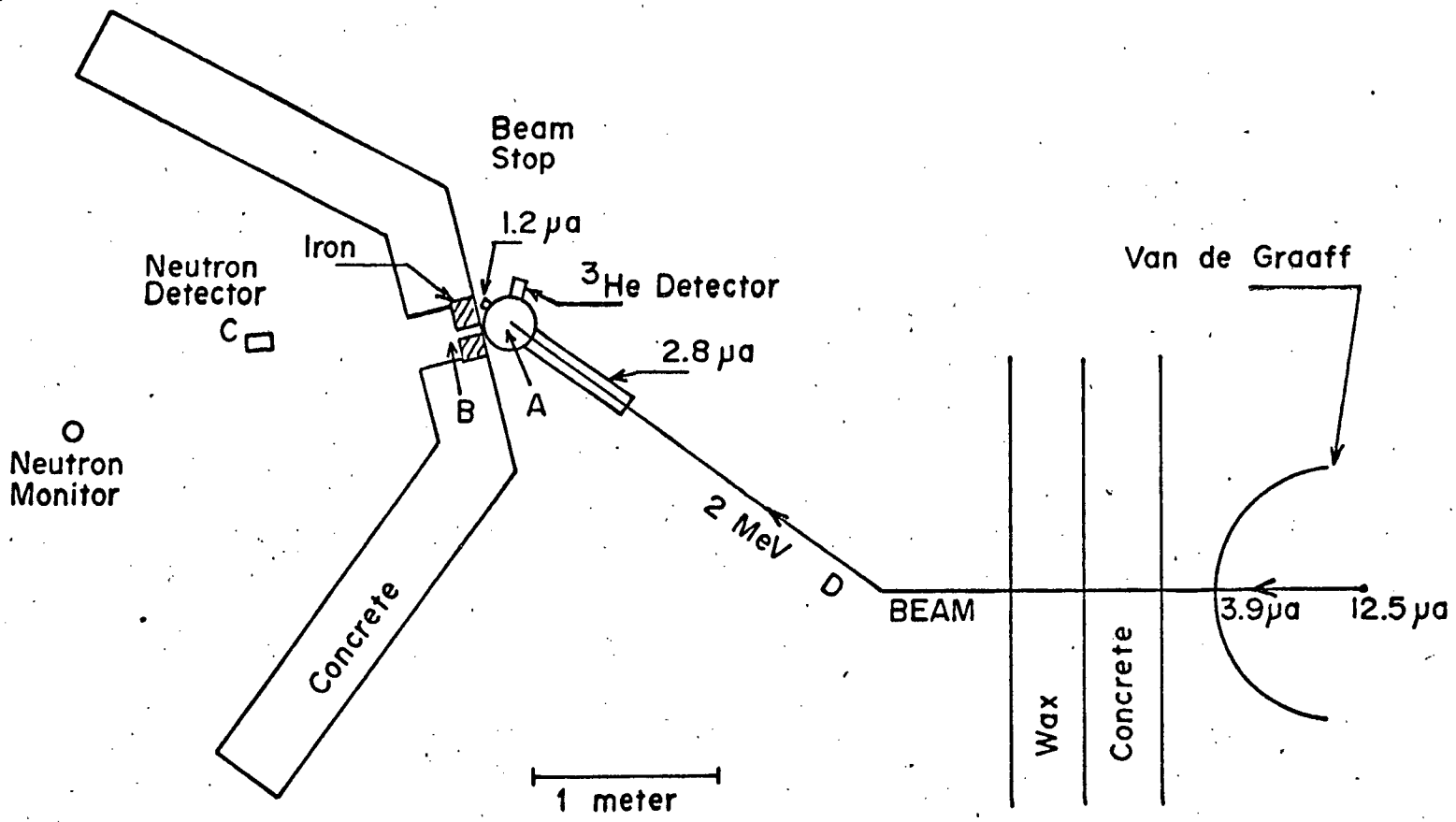

Figure 2-3 Experimental Arrangement

and lead was constructed around the neutron scattering area. An opening in the wall of this room permitted the neutron beam to enter the scattering area. This shielding deployment, detailed in figure 2-3, provided source shielding for the machine magnet and the beam dump, the two points where most of the beam was deposited, and area shielding for the scattering apparatus.

The scattering chamber, shown in figure 2-3, contained the deuteron beam collimators, rotating deuterium target, beam dump and charged particle detectors. It was maintained at approximately 10^{-6} Torr throughout the duration of the experiment. The collimators and beam dump were of tantalum in order to take advantage of the high nuclear coulomb barrier associated with this high Z=73 material. The d-Ta barrier is 10.5 MeV while for d-Fe it is 5.1 MeV. The deuteron beam collimators produced a beam spot 2 mm in diameter. The baffles in the collimator system were incorporated in order to suppress any extension of the beam beyond its 2 mm diameter. This would have arisen from small angle beam scattering from the collimator and skimmer. The sensitivity of a small angle neutron scattering experiment to this effect arises because of the necessity of placing the neutron detector as close as possible to the neutron beam. Further, only about one neutron in 10^3 or 10^4 is scattered from the sample. Hence any neutrons falling outside the beam diameter which are time correlated with ^{3}He recoil particles represent a serious source of background.

The neutron beam exit port on the scattering chamber was of 0.010" thick aluminum, 4" in diameter. This window was fabricated from an aluminum pressing, a section of a hemisphere in shape, with a "lip"

allowing an "O" ring vacuum seal to be used with an appropriate flange. These pressings are manufactured as rupture-type overpressure safety relief valves. A 0.010" aluminum pressing of this shape ruptures at a pressure differential of 40 lb/in^2.

The neutron detector (C) in figure 2-3 was mounted on a floor stand of light aluminum with provision for leveling. An aluminum channel arm (ABC) passed underneath the center of the neutron detector. This arm had lockable pivots at A and B. For the neutron beam profile the neutron detector was pivoted about A which lay under the scattering chamber center and the $D(d,n)^3He$ reaction center. For scattering experiments the neutron detector was pivoted about B which lay under the scattering sample center.

The deuteron beam collimator, deuterium target, ^3He recoil particle detector, and neutron detector were aligned using a theodolite and Helium-Neon laser.

2.3.1. Deuterated Polyethylene Targets

The use of transmission deuterium targets had several advantages. A significant advantage was the elimination of scattered deuterons arising from any target supporting material. This reduction in particle intensity allowed the ^3He recoil particle detector to view the target directly. In the absence of scattered deuterons from target supports, no magnetic analysis to separate ^3He particles was necessary. Thus both charge states, 15% $^3He^+$ and 85% $^3He^{++}$, at 1 MeV, were detected. These arise within a few atomic layers of the target and hence are present

in equilibrium ratio even with the use of thin targets. Moreover, the fact that the deuterated polyethylene target was thin both to incident deuterons, ΔE=0.32 keV/μgm/cm^2, and to ^{3}He recoil particles, ΔE=2.7 keV/μgm/cm^2, ensured that transit time spreads and kinematic broadening due to energy losses in the target were minimized. Finally, no foil was used to screen the ^{3}He recoil particle detector, so this possible source of timing spread was also avoided.

The targets were manufactured by dissolving Deuterated Polyethylene $(CD_2)_m$, a long chain polymer, in boiling Xylene. The concentration used was $3x10^{-3}$ gm. D-Poly. per ml. Xylene. The solution was held near the boiling point, 140^o, until the visible flakes of polyethylene dissolved, usually about three minutes. The solution was allowed to stop boiling. It was then poured out on to 3 inch by 3 inch chemically polished glass slides. These were "Micro Slides" manufactured "process clean" by Corning Glass Works, Corning, N.Y., U.S.A. The polyethylene covered slides were allowed to cure for 24 hours.

Thin, 10 micro gm/cm^2, carbon films were employed on both faces of the target to effect a "sandwich" configuration. These layers of carbon were deposited in vacuum by carbon arc evaporation. The first layer was laid on the glass slide, the second on the surface of the hardened polyethylene. These carbon layers stabilized the target against deuterium loss, (Ma 69), (McF 73).

Finally the target material was floated on to a water surface. Scratching the glass slide along the edge was necessary to cut the polyethylene free. The slides were then lowered edge first at an angle of approximately 45^o into the water, the target material floating free.

For a 3 inch by 3 inch slide this operation typically required 15 minutes. Target holders were used to pick up sections of the target material, which was then allowed to dry.

2.3.2. Rotating the Targets

The major difficulty in the use of these thin deuterated polyethylene targets was that of mechanical stability under deuteron beam bombardment. This problem was solved by the design of a rotating target system for 0.75" diameter targets (McF 73).

Figure 2-4 shows a diagram of the rotating target assembly attached to the top cover (A) of the scattering chamber. A Balzers (Model 65013) high speed rotary vacuum seal (B) with its axis of rotation along the Z-axis imparted its rotational motion to the "O" ring as indicated. This rotational motion was transferred by frictional coupling to the deuterium target holder mount (D) which lay in the Z-X plane, mounted on "aircraft type" bearing (C). Its axis of rotation was along the Y-axis. The target holders were attached to the target holder mount and centered by positioning pins. The incident deuteron beam lay in the X-Y plane and, depending on the disposition of detectors within the scattering chamber, intercepted the plane of the target at an angle to produce the elliptical beam spot as shown.

Except during angular acceleration up to an operational speed of 7 cps, the targets were subjected to constant mechanical stresses. The design and construction emphasized overstrength materials and close tolerances. Difficulties arising from mechanical stresses and vibrations

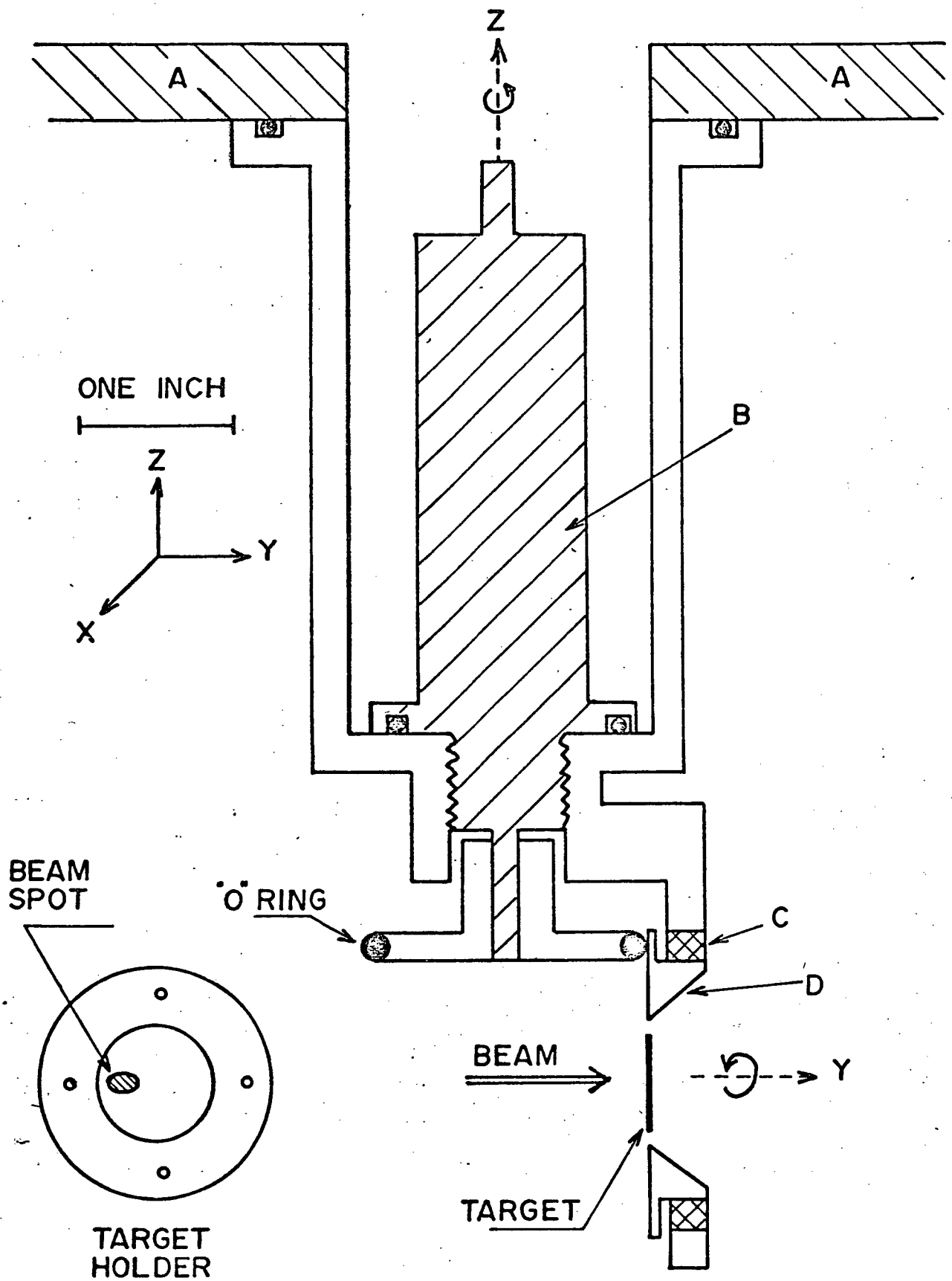

Figure 2-4 Rotating Target Mechanism

were successfully eliminated with the design.

2.3.3. Target Lifetime

Deuterated polyethylene targets are characterized by an extremely rapid decrease in deuterium content immediately upon exposure to a charged particle beam. Makosky and Hojvat (Ma 69) reported a decrease in deuterium content of 93% during the first 300 μcoul of bombardment by a 0.7 MeV ^{3}He beam. Furthermore, most of this loss occurred during the first 20 μcoul of beam current.

Similar target behavior has been observed with a 2.0 MeV deuteron beam. Figure 2-5 shows the target yield as a function of integrated beam current in thousands of μcoul. The yield is expressed in terms of the thickness of deuterated polyethylene target required for that yield assuming no deterioration of the target has taken place. Thus, after 50×10^3 μcoul, the target has a yield equivalent to an unchanged target of 15 μgm/cm^2 deuterated polyethylene. Note that the region where most loss occurs, the first 1000 μcoul, is not resolved here.

Figure 2-5, which is representative of the targets used in the present experiment, shows for a current of 1.5 μamp. of 2.0 MeV deuterons a target lifetime in excess of 200×10^3 μcoul. Target losses arising from mechanical failure were infrequent.

2.4. ^{3}He Recoil Detector

A Nuclear Triode* was used to detect the ^{3}He recoil particles.

*Manufactured by Nuclear Diodes Inc., Prairie View, Ill., U.S.A.

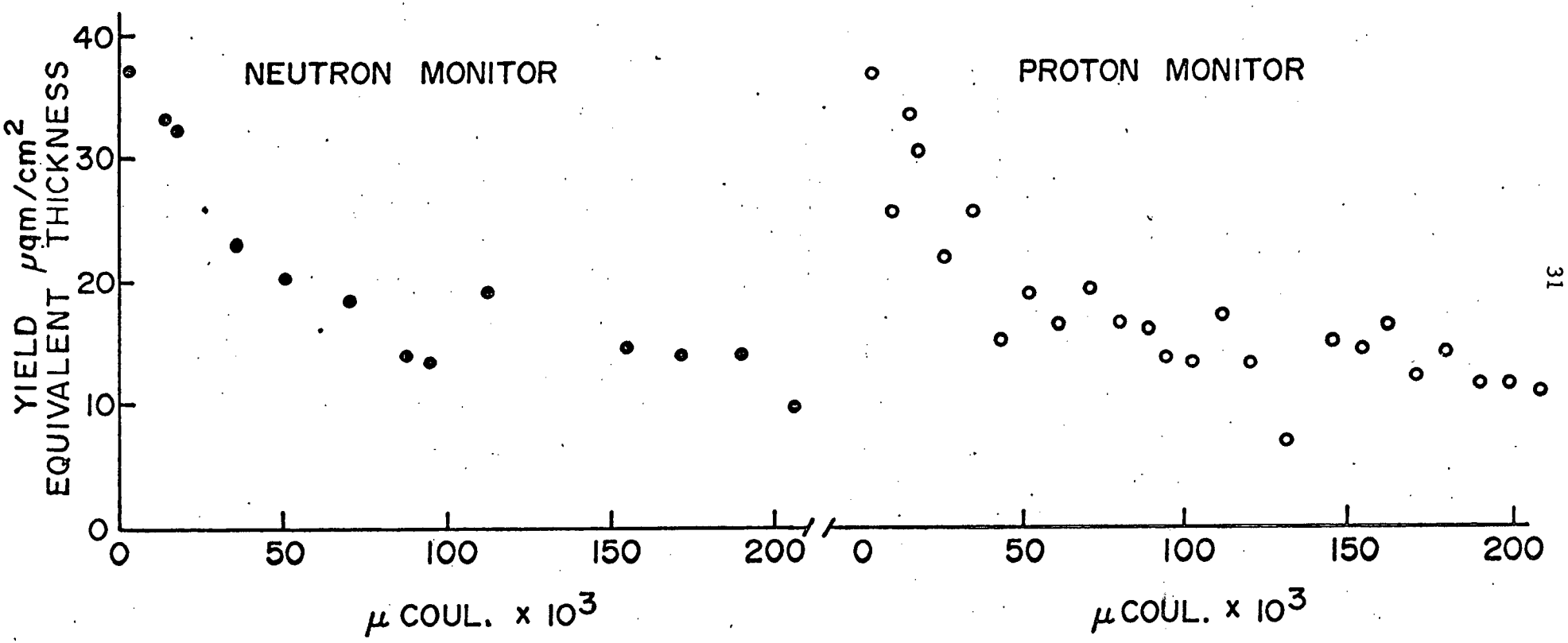

Figure 2-5 Deuterium Target Yield vs. Integrated Beam Current

This type of silicon surface barrier detector allows energy spectroscopy and timing signal derivation to be performed in the customary manner. In addition, a position signal is available. This enables the position of impact along one axis of the detector face to be determined by an additional information channel in the electronics.

The detector is essentially a large area semiconductor diode consisting of a 450 micron p-type silicon layer on a thicker 4 mm x 20 mm wafer of n-type silicon. A thin, 40 $\mu gm/cm^2$, layer of gold provides electrical contact over the detector face. Contact is also made to the substrate silicon wafer. The diode junction is reverse biased (-100 V). The passage of a charged particle gives rise to electron-hole pairs and a current pulse proportional to the energy deposited in the detector is produced.

In the Nuclear Triode, the silicon wafer is provided with electrical contact at its two ends. The resistivity of the silicon wafer is chosen such that it acts as a resistive divider for the detector current pulses. The resistance of each arm of the current divider is directly proportional to the distance from the point of particle impact to the edge of the detector along the longer axis. The linearity of this relationship is maintained within 7% over the detector face.

The current appearing at one wafer contact is returned to ground. The current appearing at the other wafer contact is:

$$P = (X/L)\,E \tag{2-1}$$

Here E is the energy current, X the distance from the contact edge that the particle impacts, and L the detector length.

2.5. Neutron Detector

The neutron detector used to study the neutron beam characteristics was a thin slab liquid scintillator manufactured by Nuclear Enterprises Inc. A scintillating fluid, NE218, was encapsulated in a rectangular aluminum extrusion, 1 inch x 4 inch x 4 inch deep. The interior surfaces were painted with titanium dioxide in an epoxy resin base in order to obtain a high reflectance. The scintillator was viewed by a Phillips 56 AVP photomultiplier tube. A short, 2 inch, light pipe of lucite matched the rectangular geometry of the scintillator to the circular geometry of the photomultiplier tube. Dow Corning 20-057 clear viscous silicone fluid was used for optical coupling. These three components were housed in an aluminum case.

The scintillating fluid, NE218, was chosen on the basis of two considerations. First, it is similar to other available liquid scintillators in decay time of the light pulse, 3.9×10^{-9} sec, and hydrogen to carbon ratio, 1.397. Second, it possesses superior neutron-gamma pulse shape discrimination capabilities (Re 66). The neutron-gamma ray pulse shape discrimination circuitry is described below.

In appendix 1, discussion of the calculation of neutron scintillation detector efficiencies is presented. For the scintillator described here the calculated efficiency was $\varepsilon = 44\%$ for incident 4.3 MeV neutrons with a threshold of 260 keV.

2.6. Electronics

The configuration of the electronic circuits used in the neutron

beam study and the scattering experiment is shown in the block diagram of figure 2-6. This circuit allowed the simultaneous analyses of the n-^{3}He time-of-flight difference, ^{3}He recoil energy, and ^{3}He position of impact to be performed.

Time-of-flight (TOF) analysis required timing pulses to be derived from the neutron and ^{3}He channels. The neutron detector photomultiplier was mounted on an ORTEC 260 Photomultiplier Timing Discriminator and PreAmplifier (TDPA). An anode and discriminator derived a fast negative pulse which was fanned out by a Pulse Shaper and presented to the start input of an ORTEC 437A Time-to-Amplitude Converter (TAC), operated on the 100 ns range. The stop input to the TAC was derived from the Constant Fraction Timing Discriminator in the ^{3}He channel. The TAC unipolar output was delayed by an ORTEC 427 Delay Amplifier (DA) and presented to the first EG&G 128BN Analogue-to-Digital Converter (ADC).

The Nuclear Triode energy pulse from the preamplifier was amplified and shaped by an ORTEC 435A Active Filter Amplifier. An ORTEC 438 Baseline Restorer (BR) prepared the pulse for the second ADC. The Nuclear Triode position pulse was analyzed by a second channel in the same manner as the energy pulse and presented to the third ADC.

In order to develop a logic pulse to instruct the ADC to analyze an event, two levels of coincidence circuits were operated. The first level was a fast coincidence with a resolving time of 100 ns full width. In the neutron channel, a linear energy signal from the preamplifier was amplified and shaped to bipolar form by an ORTEC 410 linear amplifier. A Canberra Industries 1435 Timing Single Channel Analyzer (TSCA) derived a timing signal from the zero crossover point of this bipolar pulse and

SCHEMATIC ELECTRONICS

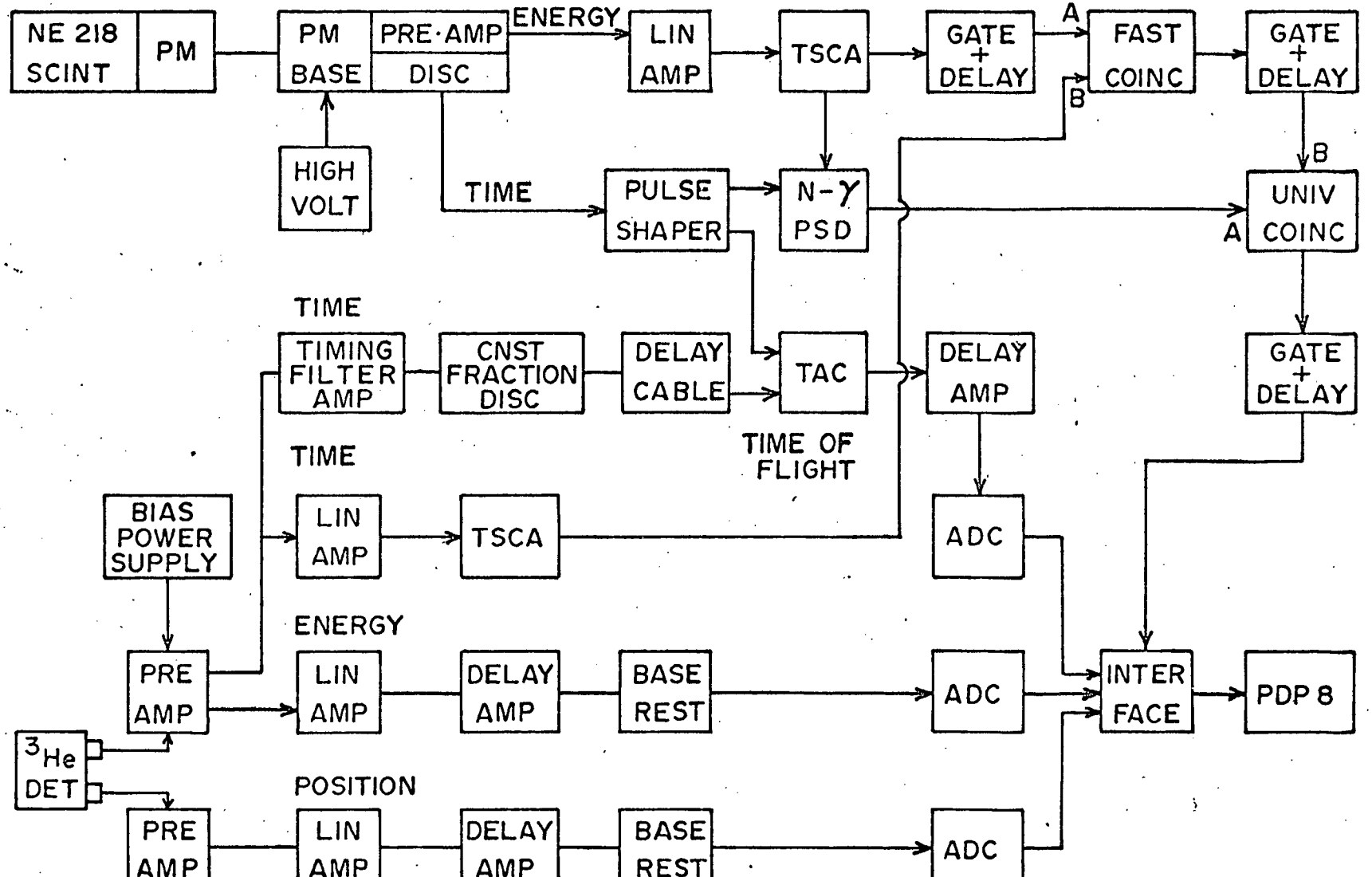

Figure 2-6

after an appropriate delay this passed to the input of a Lecroy Research System 3B coincidence unit. Similarly, the ^{3}He preamplifier signal was amplified and shaped by a Linear Amplifier (LA), a timing signal developed by the TSCA, and presented to the second fast coincidence input.

At the second level of coincidence logic the output of the fast coincidence was delayed and presented to an ORTEC 418 Universal Coincidence. The second input here was a "neutron" pulse from the neutron-gamma ray pulse shape discrimination circuit. This coincidence was operated at a resolving time of 800 ns. Its output was delayed and presented to the ADC-PDP8 Computer interface to instruct the ADC's and computer to accept and analyze the three linear signals from the TOF, energy, and position channels.

2.7. Proton Monitor

The proton yield from the reaction d(d,T)P is proportional to the target deuterium content and the deuteron beam current. This yield was monitored for normalization purposes.

A silicon surface barrier detector was placed at an angle of 105^{o} relative to the incident deuteron beam. At 78 mm a 0.76 mm collimator subtended a solid angle of 0.302×10^{-3} sr. As shown in the proton spectrum of figure 2-7a, the detector separated the 3.02 MeV D(d,T)P protons from the 3.96 MeV $d(C^{12},C^{13})P$ protons. Lower energy elastically scattered deuterons, Tritons and ^{3}He were degraded by an aluminum foil in front of the detector face.

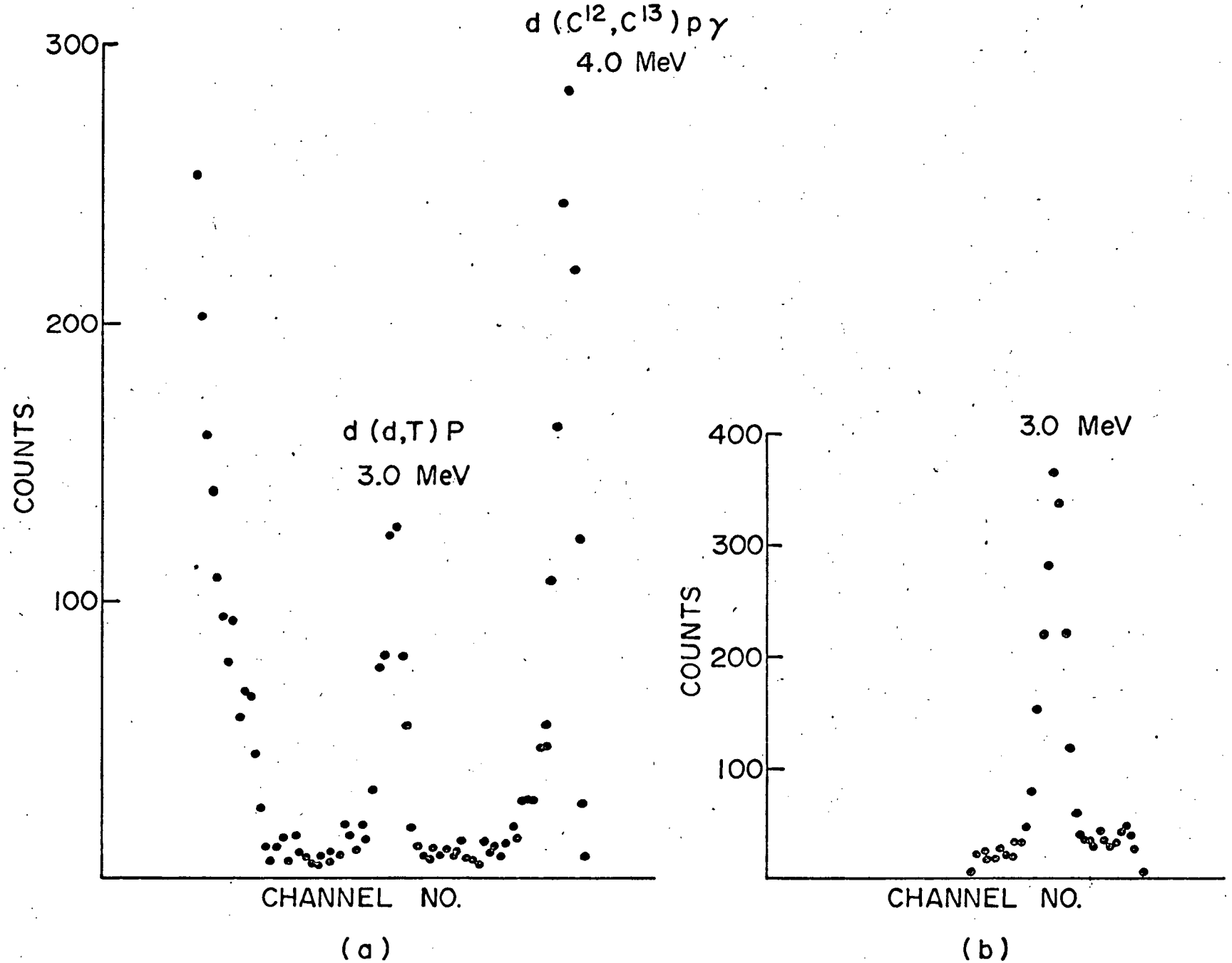

Figure 2-7 Ungated and Gated Proton Monitor Spectra

The electronic circuits associated with the proton monitor are shown in the block diagram of figure 2-8. A gated proton spectrum is shown in figure 2-7b.

A linear background subtraction was made for the proton monitor spectra. The peak was fitted to a gaussian distribution and the area obtained from this fit.

2.8. Neutron-Gamma Ray Pulse Shape Discrimination

The neutron-gamma ray pulse shape discrimination was of the leading edge-zero crossover type. This technique is based upon the fact that NE218 scintillator light pulses produced by neutrons and gamma rays have respectively lower and higher fractions of high frequency components. This means that a gamma-ray bipolar pulse (due to recoil electrons) crosses the baseline at an earlier time than a pulse (due to recoil protons) produced by a neutron. In practice, it is possible to measure this time difference with a TAC as shown in figure 2-9a.

The linear amplifier shapes the preamplifier output to a bipolar pulse. A TSCA derives a fast negative timing pulse from the zero crossover point and this is used to start the TAC. A reference timing signal is generated by a fast negative anode pulse and then delayed to stop the TAC. The TAC spectrum is shown in figure 2-9b. The poor separation of neutron and gamma-ray pulses evidenced here is almost certainly a result of inferior light collection in the thin rectangular scintillator. A TSCA was used with lower and upper discriminator levels set to accept all neutron TAC pulse heights and to reject most of the

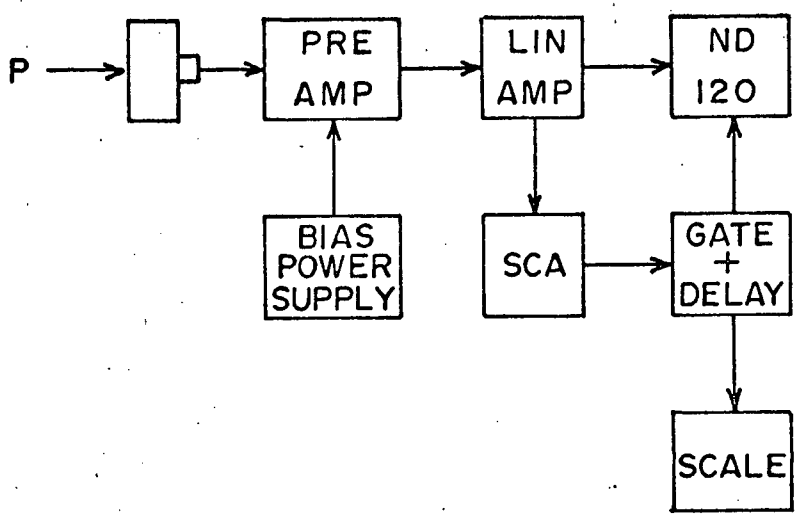

PROTON – MONITOR

Figure 2-8

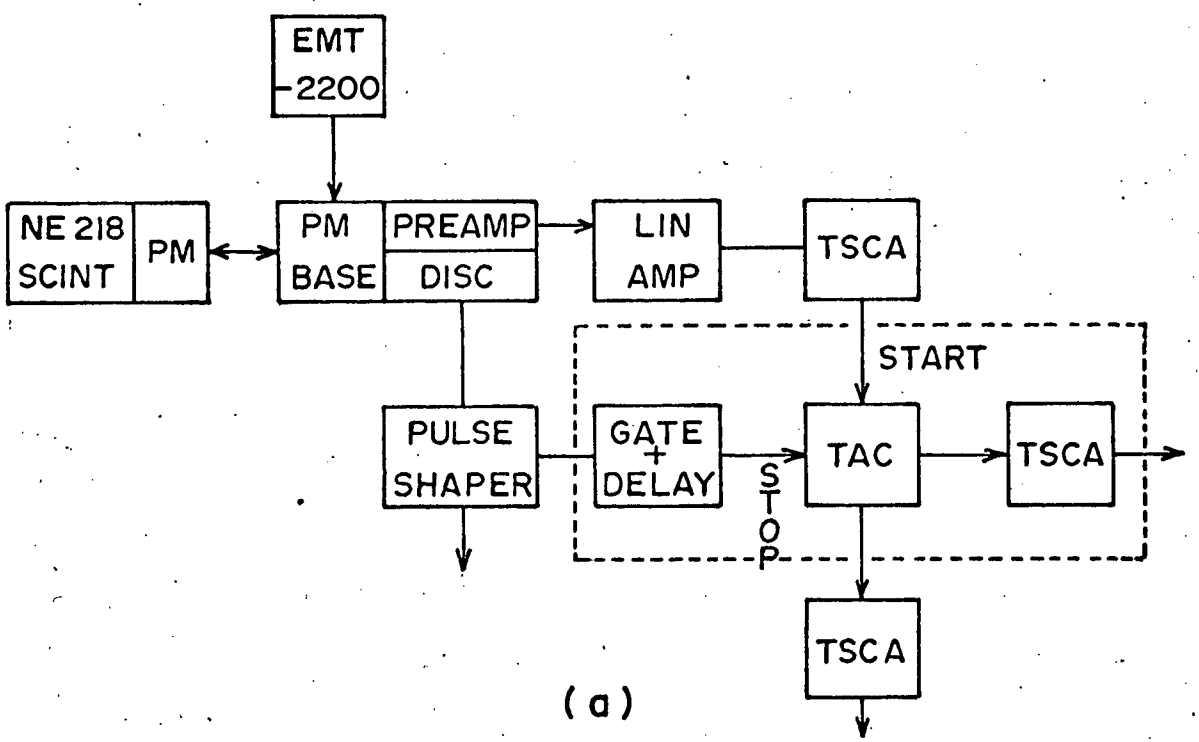

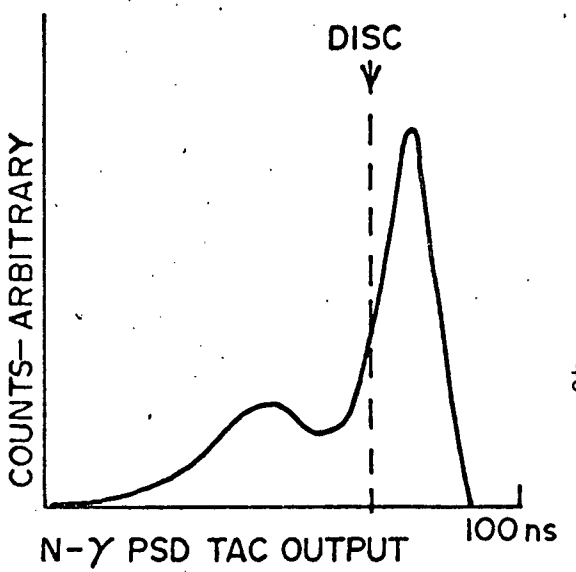

NEUTRON-GAMMA RAY PULSE SHAPE DISCRIMINATION (N-γ PSD)

Figure 2-9

gamma-ray events as shown. The TSCA output was the neutron logic pulse used in the second level of coincidence of figure 2-6.

2.9.1. Horizontal Neutron Beam Profile

The horizontal neutron beam profile was taken by pivoting the neutron detector about the $D(d,n)^3He$ reaction center. Counts were obtained at 1^o intervals. The neutron detector was oriented such that its 1 inch face subtended an angle of 0.8^o in the horizontal plane. The profile obtained, normalized to the proton monitor, is shown in figure 2-10. The solid line curve is the profile expected from the detector geometry and reaction kinematics. The discrepancy is attributed to a change in efficiency of the ^3He recoil particle detector near the edge. Systematic errors were minimized in this measurement of the profile, by alternating points on the profile left and right of the center position.

The horizontal neutron beam profile is shown in figure 2-11 on a semilogarithmic scale for angles out to 15^o. The slope of the profile between 3^o and 5^o determined the minimum angle at which the detector was placed during the scattering experiments, namely, 5^o. The rise was too rapid to permit the detector to be placed closer.

2.9.2. Vertical Neutron Beam Profile

A vertical neutron beam profile was taken with the neutron detector subtending an angle of 0.8^o in the vertical plane. The detector was then

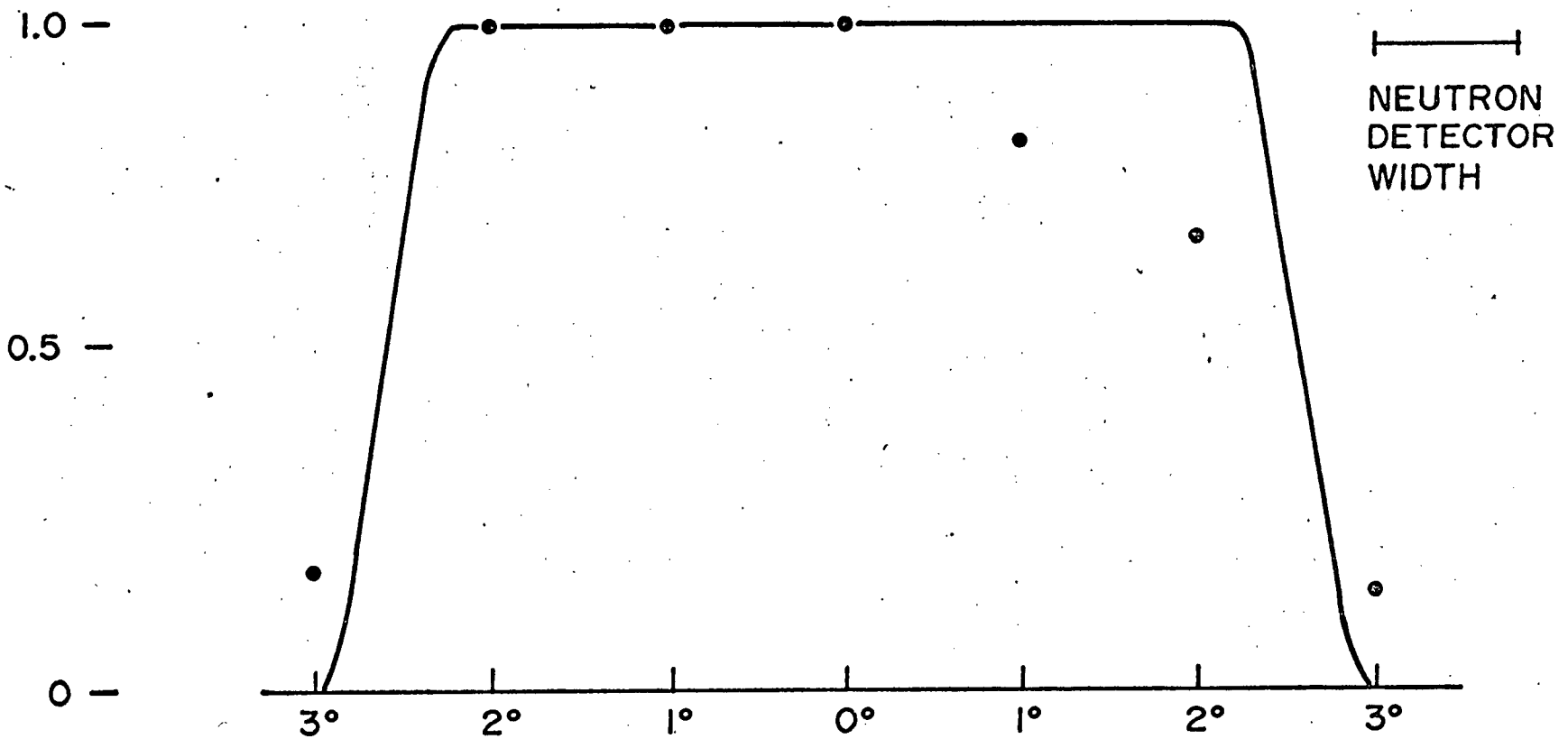

Figure 2-10 Horizontal Neutron Beam Profile

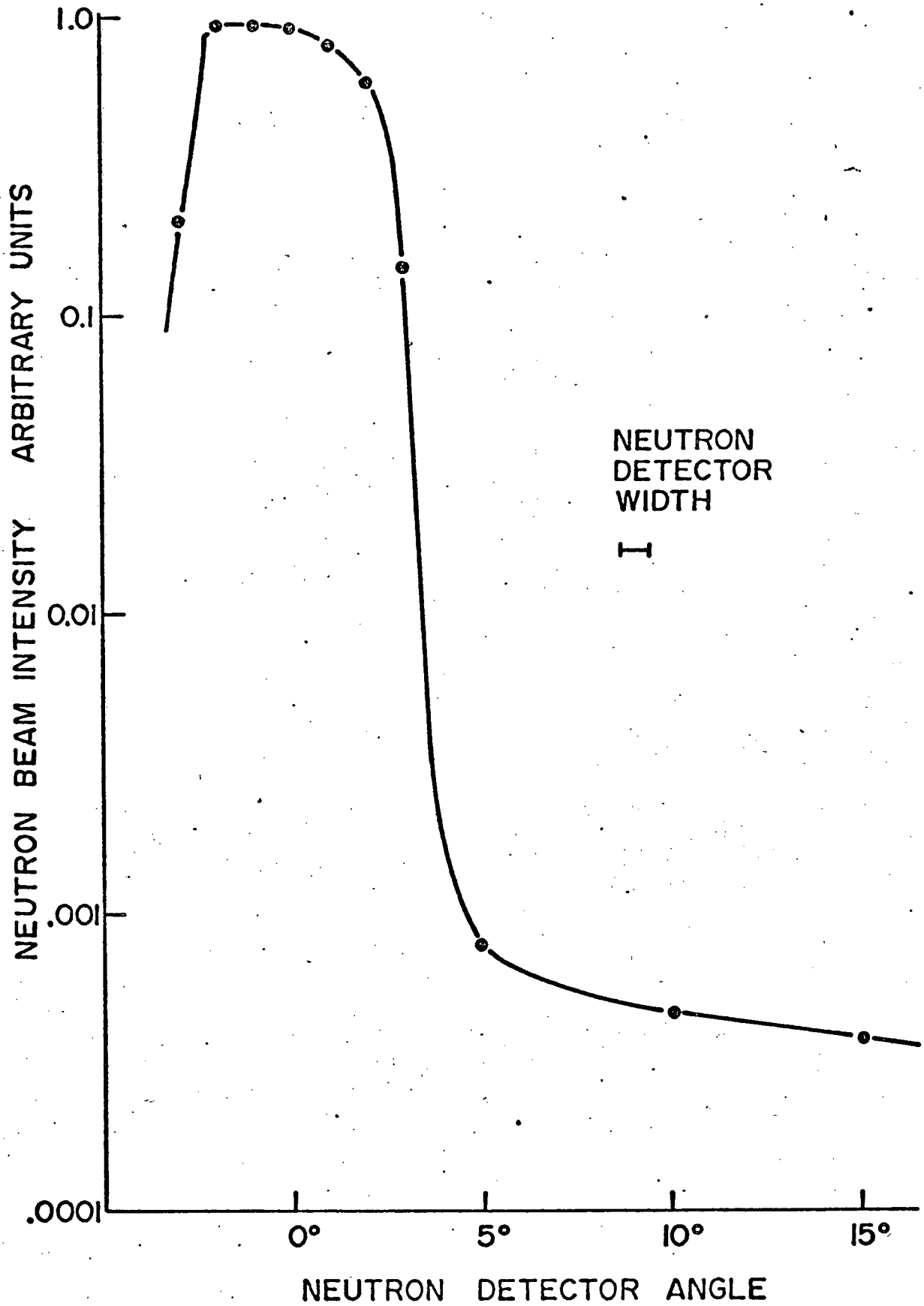

Figure 2-11 Horizontal Neutron Beam Profile

passed across the neutron beam, counts being taken at 0.8^{o} intervals. The profile obtained, normalized to the proton monitor, is shown in figure 2-12. The solid curve is that expected from the geometry of the ^{3}He detector and deuteron beam spot.

2.10.1. Use of the Position Sensitive Detector

The information carried in the Nuclear Triode position channel may be used to subdivide the horizontal neutron beam profile. Corresponding to each position of impact on the Nuclear Triode longer axis is a ^{3}He recoil angle which identifies an outgoing neutron angle through the reaction kinematics. By taking the position spectrum at each point in the horizontal beam profile, the angular resolution of the position channel may be found as in figure 2-13. The position peak width of 2^{o} results from:

$$\Delta\theta^2_{peak} = \Delta\theta^2_{beam} + \Delta\theta^2_{\substack{neutron \\ detector}} \qquad (2\text{-}2)$$

For a 0.8^{o} neutron detector angle the beam resolution is 1.8^{o} fwhm.

Unfortunately, the count rates achieved in the scattering experiments did not allow sufficient neutrons to be accumulated so that the position sensitive detector could have been exploited. Its potential has been demonstrated (McF 71) and, with an increase in neutron beam intensity coupled with some improvement in the edge of the neutron beam profile, could be profitably used at small angles.

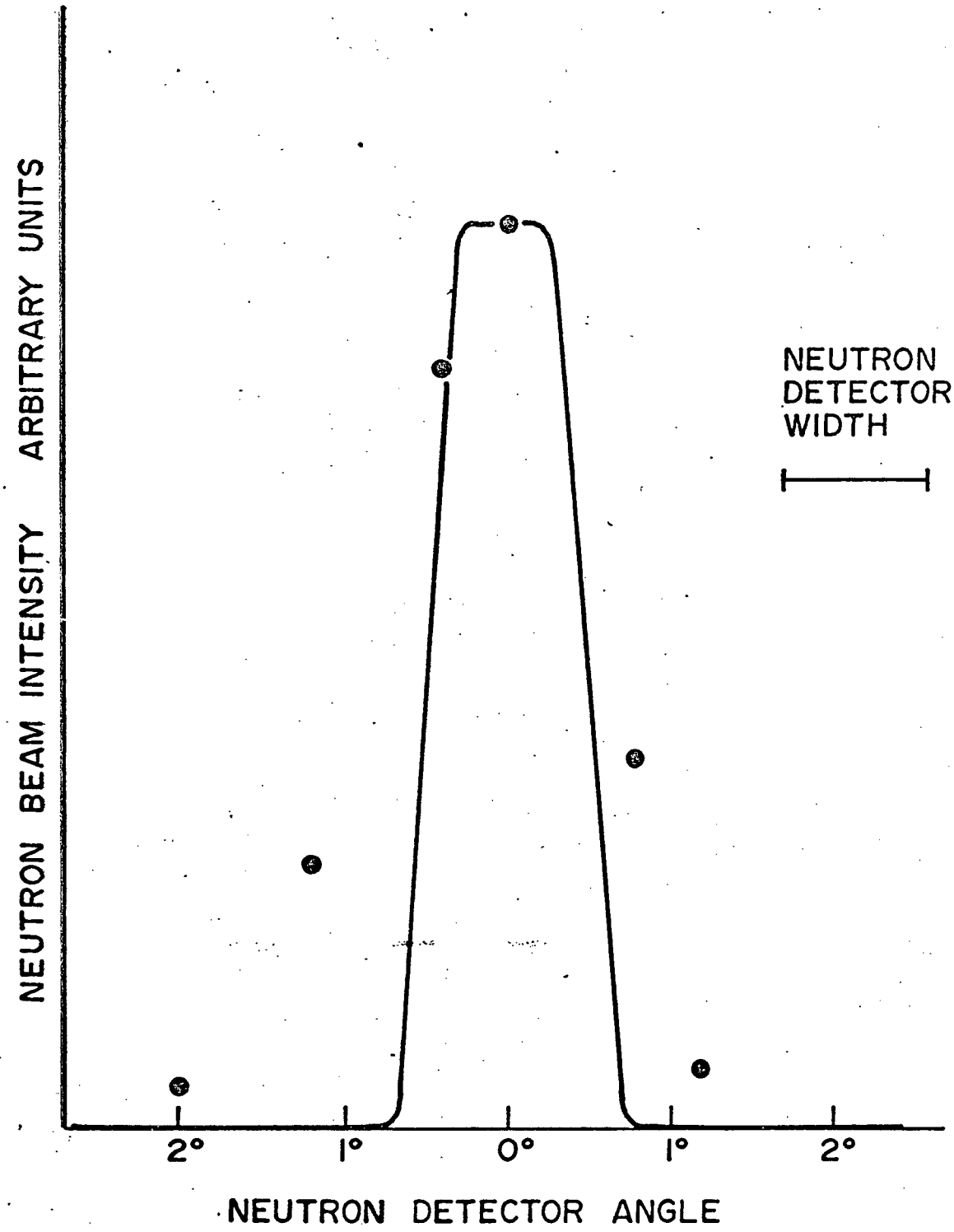

Figure 2-12 Vertical Neutron Beam Profile

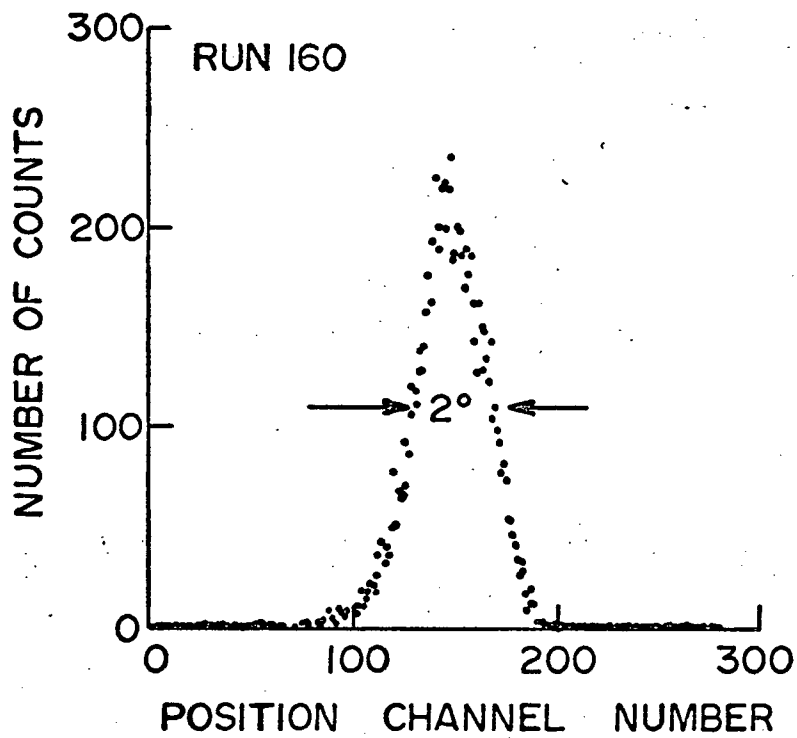

Figure 2-13 Position Sensitive Detector Spectrum.

CHAPTER 3

Scattering Experiment

Introduction

The scattering experiment utilized the neutron beam described in the previous chapter. A neutron detector was used to obtain scattered neutron counts at the angles of 5^{o}, 10^{o}, and 15^{o} for natural isotopic samples of lead, bismuth, and uranium. These data are presented below. For the scattering runs, a different neutron detector was used and a second neutron beam flux monitor was added.

3.1. Neutron Detector

The neutron detector used in the scattering experiment differed from the detector described previously only in the dimensions of the scintillator. The NE218 scintillating liquid occupied a volume 1.76 inches x 4 inches x 2.76 inches deep, in order to reduce transit time spread. The electronic logic and circuitry were identical with those previously used. This scintillator had a calculated efficiency of 37 % at 4.3 MeV for a threshold of 260 keV, (Appendix 1).

3.2.1. Neutron Beam Flux Monitor

The neutron beam flux monitor consisted of a 5 inch diameter x

3 inch deep NE218 scintillation detector operated in coincidence with the ^{3}He recoil particle detector. This monitor was situated at a long flight path at zero degrees, care being taken to ensure that events of the type (n,n',γ) could not contribute to the time region of interest for the sample scattered neutrons. The construction details of this detector (Me 72) are similar to those described in section 2.5. Using the circuit shown in the block diagram of figure 3-1a, the monitor time-of-flight spectrum was accumulated. The negative signal from the fast discriminator started a TAC. The stop pulse was provided by a TSCA operating on a bipolar ^{3}He energy pulse. The TAC output was shaped and amplified for presentation to a Kicksort multi-channel analyzer. A representative spectrum appears in figure 3-1b. The TOF peaks were integrated by summation.

3.2.2. Neutron Monitor-Proton Monitor Comparison

The neutron monitor and proton monitor peak integrations were each proportional to the integrated neutron beam intensity for a particular run and their ratio should ideally have been constant. For the scattering described below however, a comparison of the neutron monitor and proton monitor ratio from run to run showed a variation with an RMS value of 2.6%. Several factors could contribute to this effect. Losses in the integrated monitor peaks arose from pulse pile-up and electronic dead time which changed with the counting rates and the experimental operating conditions. Furthermore the background count rates in the three detectors involved also fluctuated independantly since the detectors

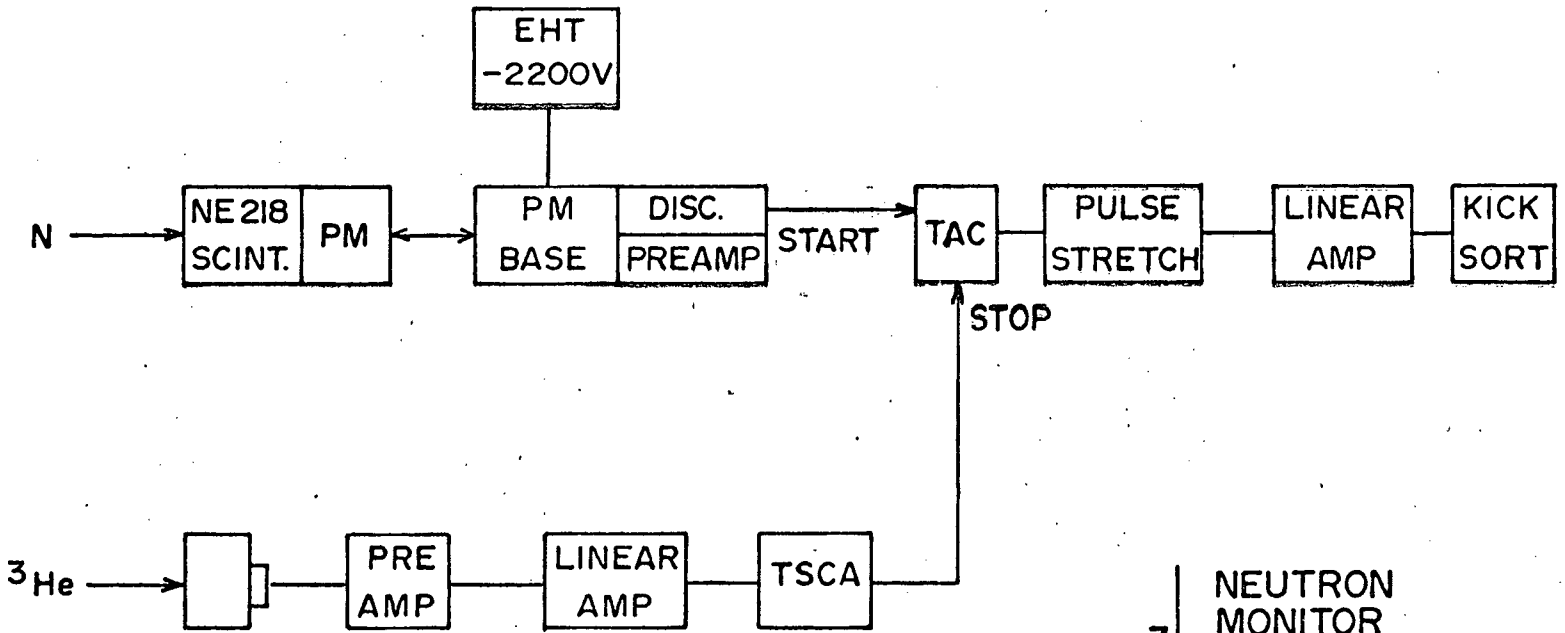

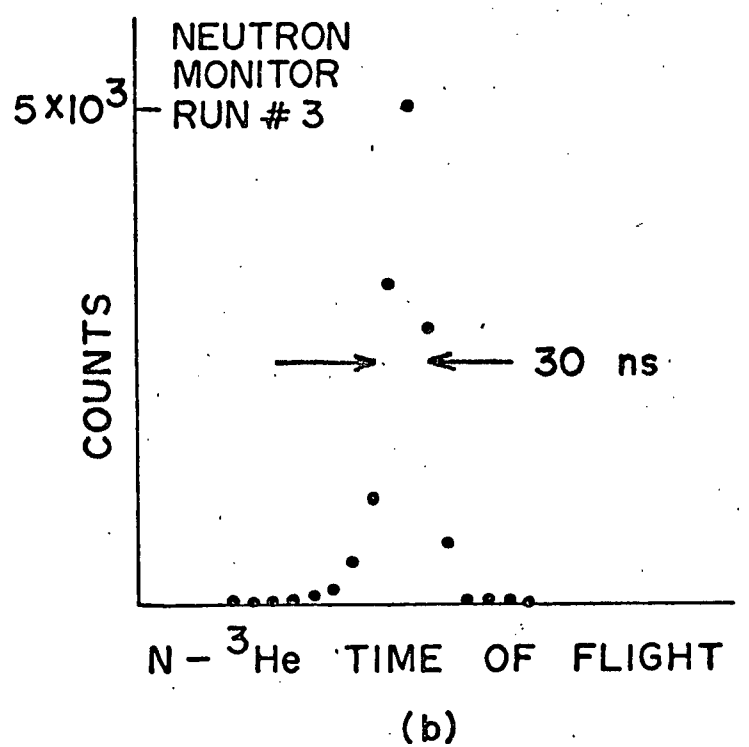

NEUTRON MONITOR

Figure 3-1 Neutron Monitor Electronics and Spectrum

were in widely separated locations.

The 2.6% monitor to monitor variation was taken as the uncertainty in the normalization of the scattering runs, the statistical error being negligible. This and the statistical uncertainty in the number of scattered neutrons detected represented the principal limits to obtaining increased precision in the measurements with the techniques described in the present work.

3.3. Scattering Samples

The scattering samples of lead, uranium, and bismuth were in the form of right circular cylinders 1.25 inches in diameter. All were 1 cm or approximately one quarter of a mean free path thick with an additional fourth sample of lead, 2 cm thick, also used. Each sample was mounted with its symmetry axis aligned parallel to the incident beam direction, and centered on the neutron beam. The samples were supported on a very light brass stand 30.0 cm from the $D(d,n)^3He$ reaction center

3.4.1. Scattering Spectra

Scattered neutrons were counted at 5^o, 10^o, and 15^o for the four scattering samples. The flight paths for the scattered neutrons were 95 cm, 135 cm, or 185 cm. The shortest flight path was used at scattering angles of 10^o and 15^o in order to increase the detector solid angle. Finite solid angle corrections were unimportant at these angles. Sample in and sample out runs were alternated.

Examples of two-dimensional ^{3}He energy time-of-flight spectra are shown in figure 3-2, sample in, and 3-3, sample out, for uranium at a scattering angle of 5^o and D_{det} = 135 cm. The time and energy spectra are shown projected on to their respective axes. The time peak width was 5.6 ns. The transit time of the neutron detector was 2.5 ns while variation in the ^{3}He and neutron flight time was 2.2 and 1 ns respectively. The residual timing error was due to electronic effects and the ^{3}He detector timing spread. These spectra are representative of the data. However, it should be noted that sample in to sample out ratio improved, i.e. increased from a value of 4 to 1 at 5^o to a value of 9 to 1 at 15^o.

The integrated spectra for all runs appear in table 3-1. The column and row titles are self-explanatory.

The times spent on sample out runs, T_o, were one third the times spent on sample in runs, T_{in}. This ratio was chosen to approximate the optimum ratio of running times

$$\frac{T_o}{T_{in}} = \left\{\frac{C_o}{C_{in}}\right\}^{\frac{1}{2}} \tag{3-1}$$

where C_o = sample out count rate

C_{in} = sample in count rate

The beam time required to obtain the spectrum of figure 3-2 was 8 hours. The experiment was operated on a 24 hour per day basis. Data was collected in the periods when suitable University of British Columbia Van de Graaff machine conditions were available over the 3 month duration of the experiment.

		5°		10°		15°	
		NEUTRON COUNTS	PROTON COUNTS	NEUTRON COUNTS	PROTON COUNTS	NEUTRON COUNTS	PROTON COUNTS
	IN	1248	303.6k	98	30.9k	184	78.7k
135 cm	OUT	105	108.9k	7	14.9k	10	39.7k
U 1 cm							
	IN			707	108.1k	1188	218.5k
95 cm	OUT	———		40	39.0k	56	86.9k
	IN	961	304.2k				
135 cm	OUT	127	123.9k	———		———	
Pb 1 cm							
	IN			802	151.4k	812	181.7k
95 cm	OUT	———		53	45.7k	64	76.8k
	IN	207	83.3k			293	140.7k
185 cm	OUT	21	37.0k	———		23	85.7k
Pb 2 cm							
	IN	643	126.9k	289	83.9k	292	87.3k
135 cm	OUT	37	43.0k	28	40.5k	14	43.5k
	IN	633	203.7k				
135 cm	OUT	92	78.1k	———		———	
Bi 1 cm							
	IN			512	113.7k	598	192.6k
95 cm	OUT	———		42	38.4k	96	106.1k

Table 3-1 Neutron Scattering Data.

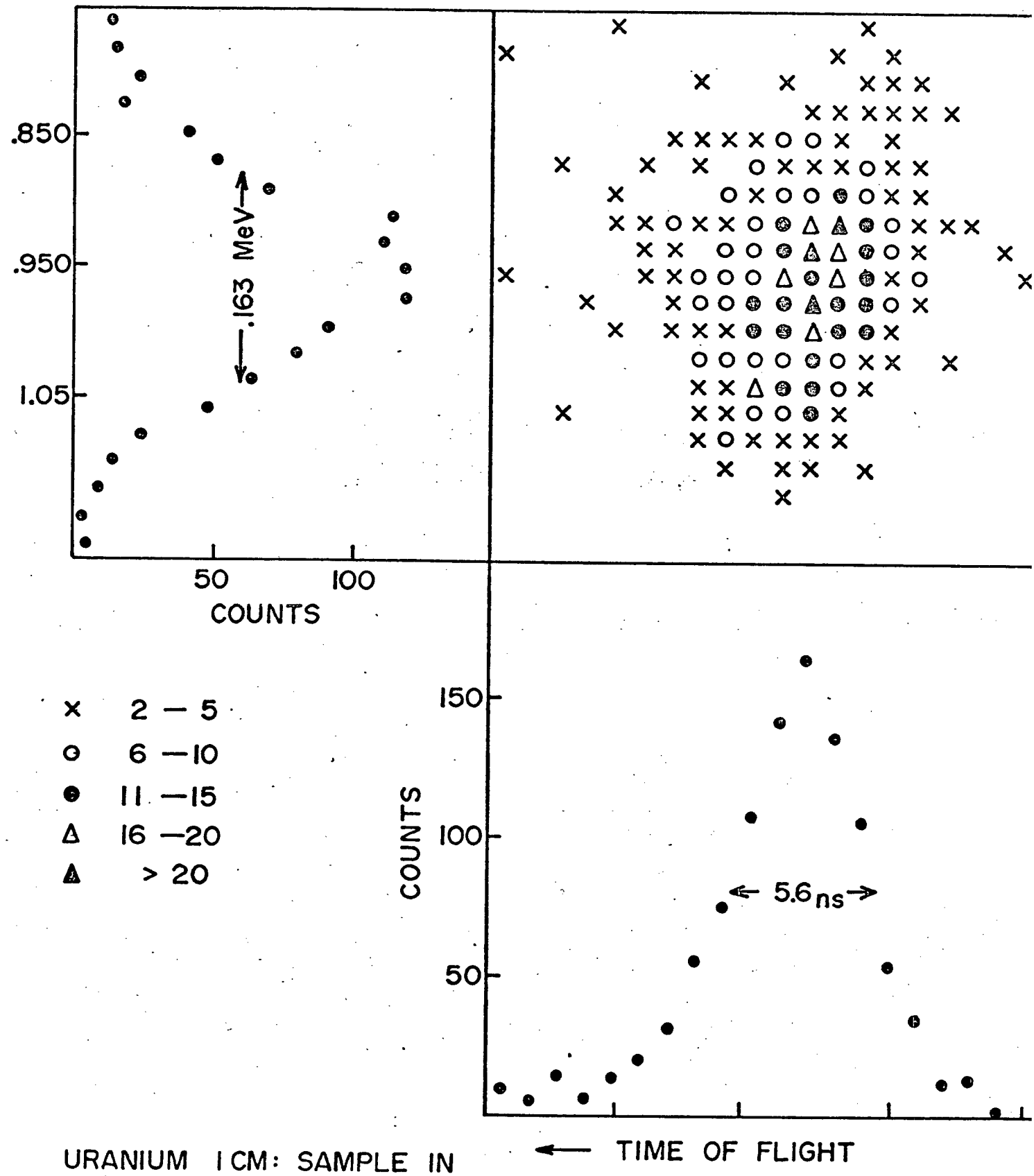

Figure 3-2 Experimental Spectrum for Uranium "Sample In"

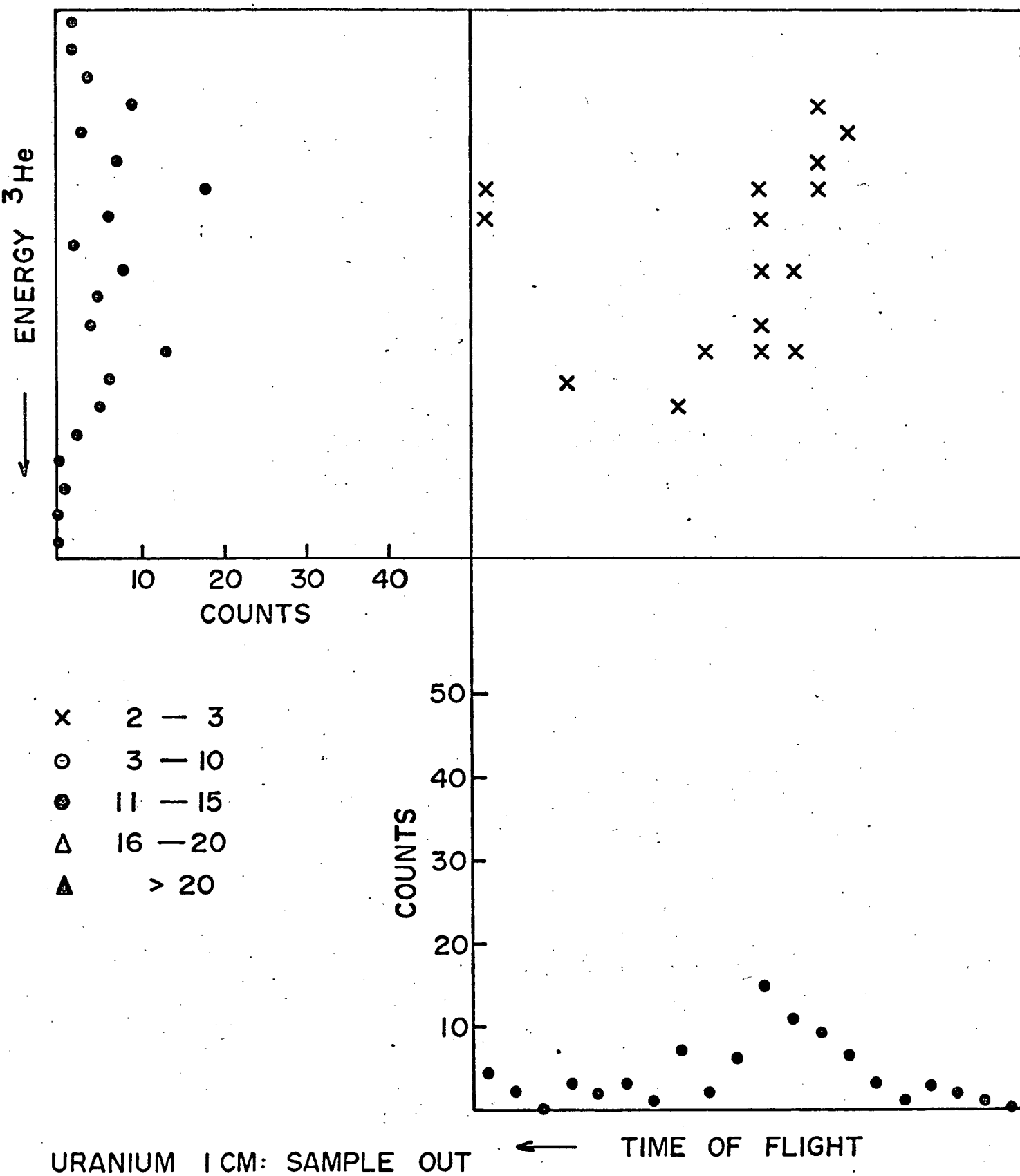

Figure 3-3 Experimental Spectrum for Uranium "Sample Out"

CHAPTER 4

Data Reduction

Introduction

The data were reduced to obtain the neutron differential cross sections, $\frac{d\sigma}{d\Omega}(\theta)$, using the relation:

$$\frac{d\sigma}{d\Omega}(\theta) = \frac{C}{N_o\ N\ \Omega\ \varepsilon} \tag{4-1}$$

where

θ = scattering angle

C = number of scattered neutrons

N_o = number of incident neutrons

N = target density

Ω = solid angle of neutron detector

ε = detector efficiency

Before these cross sections could be compared with calculated values, it was necessary to apply a background subtraction and several corrections. The data reduction and corrections are detailed below.

4.1. Normalization Procedure

The neutron counts accumulated at each position of the neutron detector were normalized to the 3 MeV proton peak from the proton

monitor. The count rates thus obtained were assigned an error based upon the counting statistics and the proton monitor - neutron monitor variation of 2.6% as discussed above.

The neutron detector was placed in the neutron beam (sample out) and C_b counts obtained. For this run, the proton monitor gave C_{pm} counts. The ratio, k, of the number of beam neutrons, N_o, to the proton monitor was just:

$$(4\text{-}2) \qquad k = \frac{N_o}{C_{pm}} = \frac{C_b}{C_{pm}\ \varepsilon\ f\ \Omega_{corr}}$$

where f = fraction of neutron beam covered by detector

Ω_{corr} = solid angle correction factor

A value of k,

$$k = 15.1 \pm 3.5\% \ ,$$

was obtained and used in the data reduction for the cross sections.

4.2.1. Air Scattering

The scattering of neutrons from the column of air lying in the neutron beam path beyond the position of the scatterer was a source of background events which could not be discriminated against on the basis of ^{3}He energy or time-of-flight information. This contribution to the background was estimated by calculation of the count rate due to a column of air extending from the scatterer position to a cut-off distance X_c. This count rate per incident neutron, A, can be written down as:

$$(4\text{-}3) \qquad A = \varepsilon \int_{X=0}^{X=X_c} dx \sum_{i=1}^{2} N_i \frac{d\sigma}{d\Omega_i} (\theta(X))\, d\Omega(X)$$

where $i = 1$ Nitrogen $\quad i = 2$ Oxygen

N_i = No. Nuclei $cm.^{-3}$

$\frac{d\sigma}{d\Omega_i}$ = neutron differential cross section at 4.3 MeV

$\theta(X)$ = neutron beam direction-neutron detector direction angle for each position X in air column

$d\Omega(X)$ = solid angle of neutron detector

ε = neutron detector efficiency

The cut-off distance X_c is a function of the neutron detector position and the maximum time-of-flight delay allowable for an event to be accepted as a valid neutron count. The time-of-flight of an air scattered neutron is the sum of the flight time along the beam to the point of scattering and the flight time from there to the neutron detector position. The second term must take into account the energy of the neutron after scattering. At X_c the flight time of an air scattered neutron exceeds by 6 ns the flight time of a sample scattered neutron.

Note that some simplifying assumptions are implicit in Eq. 4-3. They are:

(1) a delta function neutron beam profile.

(2) a cylindrical neutron detector of small diameter oriented with long axis perpendicular to plane of scattering.

The count rate sample scattered neutrons may also be calculated for each sample, and the ratio to air scattered neutrons taken.

$$(4\text{-}4) \qquad r = A/n$$

n = sample scattered neutron count rate

The reciprocal of this ratio, n/A, is shown in figure 4-1 for Uranium. Also shown are the experimentally realized ratios of sample in/sample out count rates.

The experimental ratios are lower than the calculations and indicate that background components in addition to air scattering were present. Part of this is due to random background. From the spectrum of figure 3-3, this was estimated to be 15% of the sample out count rate at 5^{o} scattering angle. In addition to the air scattered background then, a time correlated room background was present which varied slowly with the scattering angle. The probable source of this was the area of the neutron beam collimator.

The effects of air scattering could have been investigated (Ku 68) by using an evacuated neutron flight path or by introducing a filter of identical neutron transmission into the neutron beam before the collimators. These steps would become necessary for experiments at smaller angles where air scattering would present a more serious problem.

4.2.2. Background Subtraction

The sample out count rate, C_o, may be written:

(4-5) $$C_o = B + A$$

where B = Background count rate, time correlated plus random comprising both components.

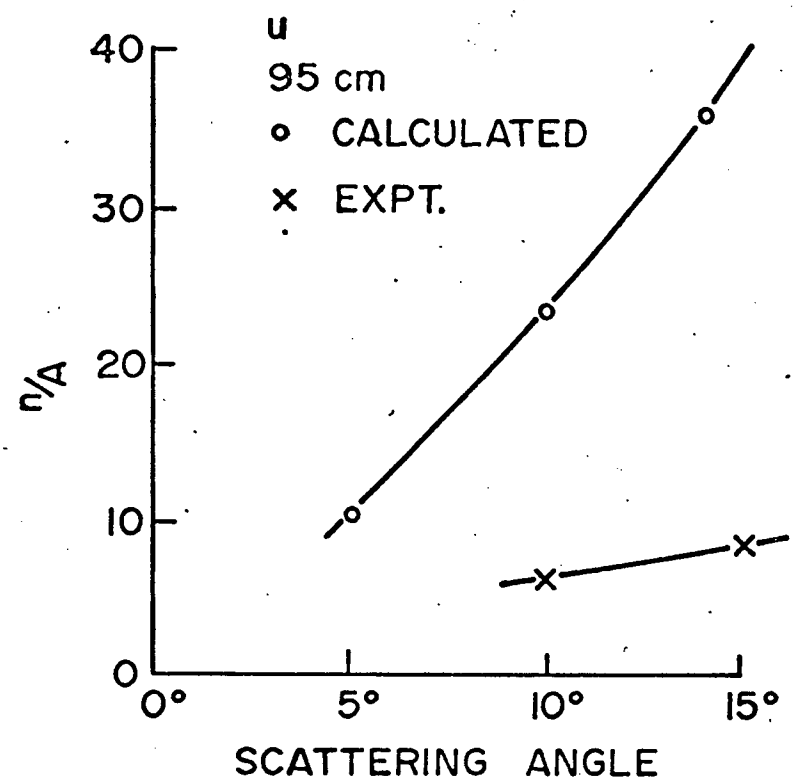

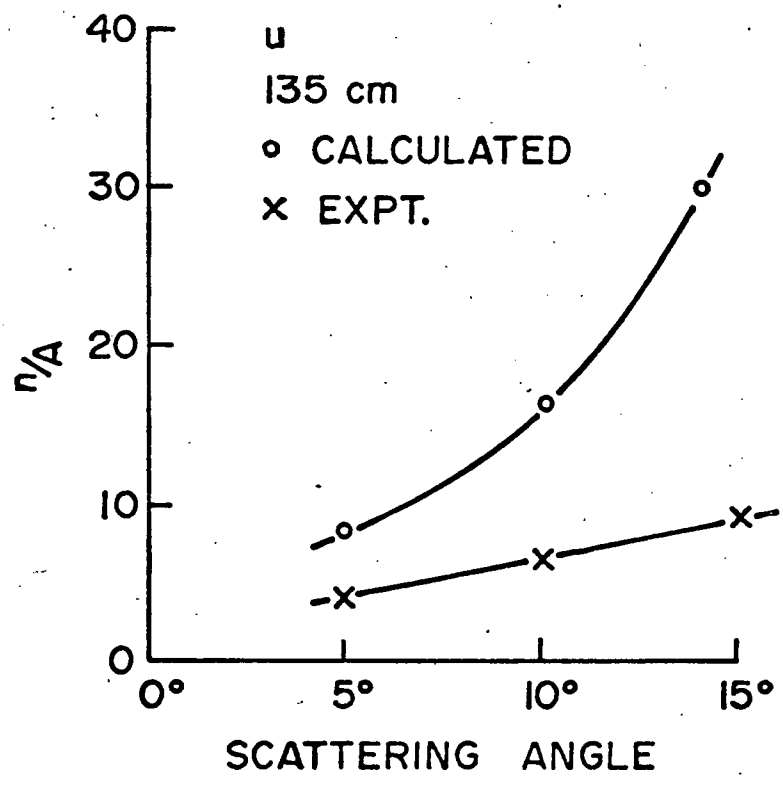

Figure 4-1 Calculated n/A Values and Experimental Sample In/Sample Out Values vs. Angle

The sample in count rate C_{in}:

(4-6) $$C_{in} = n + B + TA$$

where T = scattering sample transmission for neutrons. The transmission, T, was calculated from:

(4-7) $$T = \exp(-\Sigma t)$$

where Σ = total macroscopic cross section ($cm.^{-1}$)

and t = sample thickness (cm)

The scattering sample, when in position, attenuated the neutron beam by the transmission T and hence reduced the air scattered neutron count rate. However, the neutron beam collimator geometry was that of shadow shielding by an iron slab rather than that of a full throat. Because of this, the sample eclipsed only a fraction of the collimator surface and air volume which acted as the source of time correlated room background B. Therefore the assumption was made that the term B was unattenuated by the presence of the scattering sample.

From the above Equations,

(4-8) $$n = \frac{C_{in} - C_o}{1 + r(T-1)}$$

Using this correction the neutron count rates were found from the sample in/sample out subtraction. The correction ranged from 1% at 15^o and D_{det} = 95 cm, to 3.5% at 5^o D_{det} = 135 cm for uranium.

The experimental results shown below are only slightly affected by the background subtraction assumptions. Adoption of the other extreme hypothesis, i.e. that the entire time correlated component of B is

attenuated by the presence of the scattering sample, changes the ratio of the cross sections at 5^{o} and 15^{o} by an increase of 1.8% (of the ratio). This is incorporated into the error bars assigned to the data points.

4.3. Neutron Detector Solid Angle

For a neutron detector with detection efficiency ε, the neutron attenuation length in the scintillator, λ, is given by:

$$\varepsilon = 1 - \exp\left(-t/\lambda\right). \tag{4-9}$$

Here, t is the neutron detector depth. The effective solid angle subtended by the detector, Ω eff, is obtained from an integration over the detector volume element weighted by the attenuation neutron intensity at that element.

$$\Omega \text{ eff} = \frac{A}{t} \int_{r_1}^{r_2} dr \; \frac{\exp\left[-(r-r_1)/\lambda\right]}{r^2} \tag{4-10}$$

r_1 = distance scatterer to neutron detector front face

r_2 = distance scatterer to neutron detector rear face

A = detector area

Expressing the solid angles obtained as percent of A/r_1^2 the magnitude of the effect is:

r_1	Ω eff
95 cm	75%
135 cm	76.5%
185 cm	77%

Strictly speaking, the volume of the scattering sample should have

been integrated over, weighted by the attenuated neutron beam intensity. This would have affected the ratios of cross sections at 5^{o} to 15^{o} by less than 1% and hence was omitted.

4.4. Average Over Angular Resolution

The effect of the finite angular resolution of the neutron beam and neutron detector was to average the cross sections. From section 2.9.1., the angular width of the neutron beam was 5.1^{o} full width at half maximum. The finite scatterer to detector distance increased this to 6.2^{o}. Averaging the cross sections obtained from an optical model nuclear potential and a Schwinger interaction over this interval, left the cross sections at 10^{o} and 15^{o} unaltered. At 5^{o} the correction amounted to 1%.

4.5. Neutron Multiple Scattering

There are two effects of neutron interactions within the scattering samples which must be accounted for. The first is an attenuation of the ingoing neutron beam and of the outgoing scattered neutrons. The second is the presence, at any angle of scattering, of a count rate due to neutrons that have been sequentially scattered from two or more nuclei. These effects have been calculated for the present experiment. A discussion of the calculation may be found in Appendix 2.

The correction to the data due to the attenuation effect ranged

from 40% for the 2 cm Pb sample to 20% for the 1 cm Bi sample.

Since the samples were small fractions of a neutron mean free path, one fifth for Bi to one half for 2 cm Pb, the corrections for multiply scattered neutrons were small. The largest correction was 1.2% of the ratio of cross sections at 5^{o} and 15^{o} for the 2 cm Pb sample. This correction arose from doubly scattered neutrons. The contribution from triply scattered neutrons was demonstrably negligible.

4.6. Inelastic Contributions

Contributions to the data due to inelastically scattered neutrons can be excluded on the basis of: (1) the energy discrimination of the time-of-flight system and (2) the behavior of the excitation functions to low-lying discrete inelastic nuclear levels.

For a neutron of energy E inelastically scattered with energy E' from a nuclear level with excitation energy E*, the energy loss of the scattered neutron is (approximately, for a heavy nucleus), $E^* = E-E'$. Inherent in the time-of-flight system is an energy discrimination against neutrons with energy loss greater than E_{disc}. For the 6 ns time cut off used, the value of E_{disc} ranges from 1.22 MeV, at D_{set} = 95 cm, to 0.70 MeV, at D_{set} = 185 cm. Only nuclear levels lying below $E^* = E_{disc}$ can contribute to a contamination of elastically scattered neutron events.

A review of inelastic scattering data for ^{238}U has been made by Igarasi (Ig 70). The complete level scheme contains some 18 levels below 1.22 MeV excitation energy. The experimental excitation functions

are available for most of these levels (Bar 66) (St 65) (Ba 65) and good fits were obtained using a Hauser-Feshbach calculation. The compound inelastic excitation functions exhibit a (usually) rapid rise above the threshold energy to a maximum followed by a slower monotonic decrease to negligible value. The maximum values are in the range 1.5 barns for the first level to typically 0.2 barns although some levels are more weakly excited.

The total inelastic cross section, the sum of the cross sections of the discrete levels, thus rises with increasing neutron energy, as the excitation energies of succeeding levels are reached. The total inelastic cross section reaches a maximum of 2 barns at 1 MeV. At this excitation energy, however, the density of levels available in the residual nucleus ρ (E*) begins to become important, increasing as (Bo 69):

$$\rho\ (E^*) = \text{Cnst.} \quad \frac{\exp\ (2\ \sqrt{aE^*})}{(E^*)^2} \tag{4-11}$$

Now the continuum levels increasingly compete with the discrete levels, suppressing them at 3 MeV and above.

Thus low-lying levels not excluded on the basis of time-of-flight information contributed negligibly, less than 0.5%, to the count rate of scattered neutrons at small angles.

CHAPTER 5

Comparison with Theory and Conclusions

5.1. Introduction

Forrester (Fo 70) has considered both the nuclear and Coulomb effects in calculating the neutron differential elastic scattering cross sections for lead, bismuth and uranium at 4.3 MeV neutron energy. The interaction used the nuclear optical model and the electromagnetic Schwinger and polarizibility potentials of sections 1.2.2. and 1.2.3. above. These calculations are summarized below.

The experimental cross sections of the present work are compared to the calculations and conclusions presented. Finally some suggestions for future work are made.

5.2.1. Optical model parameters

The optical model computer code Abacus (Au 62) was used to obtain the local fixed energy optical model parameters of equation 1-4. Previously published differential elastic cross sections were available for lead (Wa 55) (Bo 54) (Ok 59) (Go 67), bismuth (Wa 55) (Th 63) (Go 67), and uranium (Wa 55) (Ba 65) (Go 67). Data in the incident neutron energy range 4.0 to 4.4 MeV and in the angular range 15^{o} to 180^{o} were fitted using the parameter search facility of Abacus. This establishes a "best fit" by seeking a minimum in the value of chi squared defined as

$$(5\text{-}1) \qquad \chi^2 = \frac{1}{M} \sum_{m=1}^{M} \left(\frac{d\sigma(\theta_m)^{Calc.} - d\sigma(\theta_m)^{expt.}}{\Delta d\sigma(\theta_m)^{expt.}} \right)^2$$

Where M = number of data points

$d\sigma(\theta)$ = differential cross sections at angle θ

$\Delta d\sigma(\theta)$ = errors associated with $d\sigma(\theta)$

First a coarse parameter scan was made to find the region of parameter space containing a minimum in χ^2. Then the Abacus parameter search facility was used in an automatic fine parameter scan to optimize the fit to the experimental cross sections.

The parameters of the optical model do not vary rapidly with neutron energy (Ho 67) and the use of an energy interval ΔE_n = 0.4 MeV is conservative. At scattering angles $\theta = 15^o$ the electromagnetic contribution to the cross section is negligible. Thus the cross sections are essentially "pure nuclear" and the optical model parameters derived from the large angle data are unambiguous in this respect. Polarization data were not considered in the optical model fit and so large angle Schwinger polarization effects (Mo 64) are also avoided here. In the case of lead, isotopic abundance effects were ignored as unimportant (Mo 68).

As in many previous optical model studies, for example (Ba 65) (Mo 68) (Go 67) (Ku 68) the compound elastic cross section was not estimated or taken into account in the fitting procedure. However estimates are available (Wi 64) (Au 64) from Hauser-Feshbach calculations (Ha 52). These calculated compound elastic differential cross sections are:

0.105 b/s lead

0.163 b/s bismuth

0.061 b/s uranium

These cross sections are not strictly isotropic (Au 64) as often assumed. However they are nearly isotropic in comparison to the diffraction pattern shape elastic differential cross sections. Inclusion of the effects of compound elastic scattering would have produced better fits to the data, especially in the regions of the diffraction minima where most of the elastic scattering is through the compound nucleus. This can be done by subtracting the Hauser-Feshbach calculated cross sections before the fitting procedure is applied. Alternatively, an isotropic component may be introduced into the least squares fitting routine. The magnitude of this is then varied to optimize the fit to the data. The subtraction of a compound elastic component before the optical model fit would have deepened the minima and thereby tended to decrease the depth of the imaginary well depth.

It is important to consider the sensitivity of the calculated cross sections, especially at small angles, to variations in the optical model parameters. Kuchnir et. al. (Ku 68) have investigated the response of the optical model calculations using the potential of equation (1-17), including both nuclear and electromagnetic interactions, to systematic variations of the parameters V, W, and V_s, one at a time. The variations were rather large, ± 50.% for V and ± 33.% for W and V_s. At scattering angles $\theta \leq 20^o$ the shape of the cross sections and polarization of scattered neutrons were insensitive to these changes. Differences were primarily of magnitude only. Changes did occur at angles $\theta \leq 20^o$. In addition, several sets of optical model parameters

were used. Again the shape of the cross sections for angles below 20^{o} were found to be model independent. These results have been substantiated by a later study (Go 70). Using an optical model potential with different sets of parameters a 2% change in the ratio of cross sections at 5^{o} and 15^{o} was found.

The optical model parameters obtained from the fit to large angle data are listed in Table 5-1.

Table 5-1

	V	W	V_s	r_v	r_w	a	b (fixed)
^{208}Pb	46.5	2.44	8.5	1.24	1.19	0.67	1.0
^{209}Bi	46.5	3.63	12.0	1.26	1.26	0.65	1.0
^{238}U	45.2	7.39	12.0	1.25	1.25	0.69	1.0

Figure 5-1 from (Fo 69) shows the quality of the fit obtained for uranium. The solid curves were calculated using the parameters of Table 5-1 and a nuclear only interaction. The data shown (for angles $\theta \geq 15^{o}$) were those used to obtain the parameters.

5.2.2. Calculation of Small Angle Cross Sections

Monahan and Elwyn (Mo 64) have developed a Born approximation suitable for the solution of a scattering problem which includes a long range potential that extends beyond the nuclear radius as does the electromagnetic interaction. In this case the total potential V(r) may be broken up into two parts $V_1(r)$ and $V_2(r)$. The potentials are defined

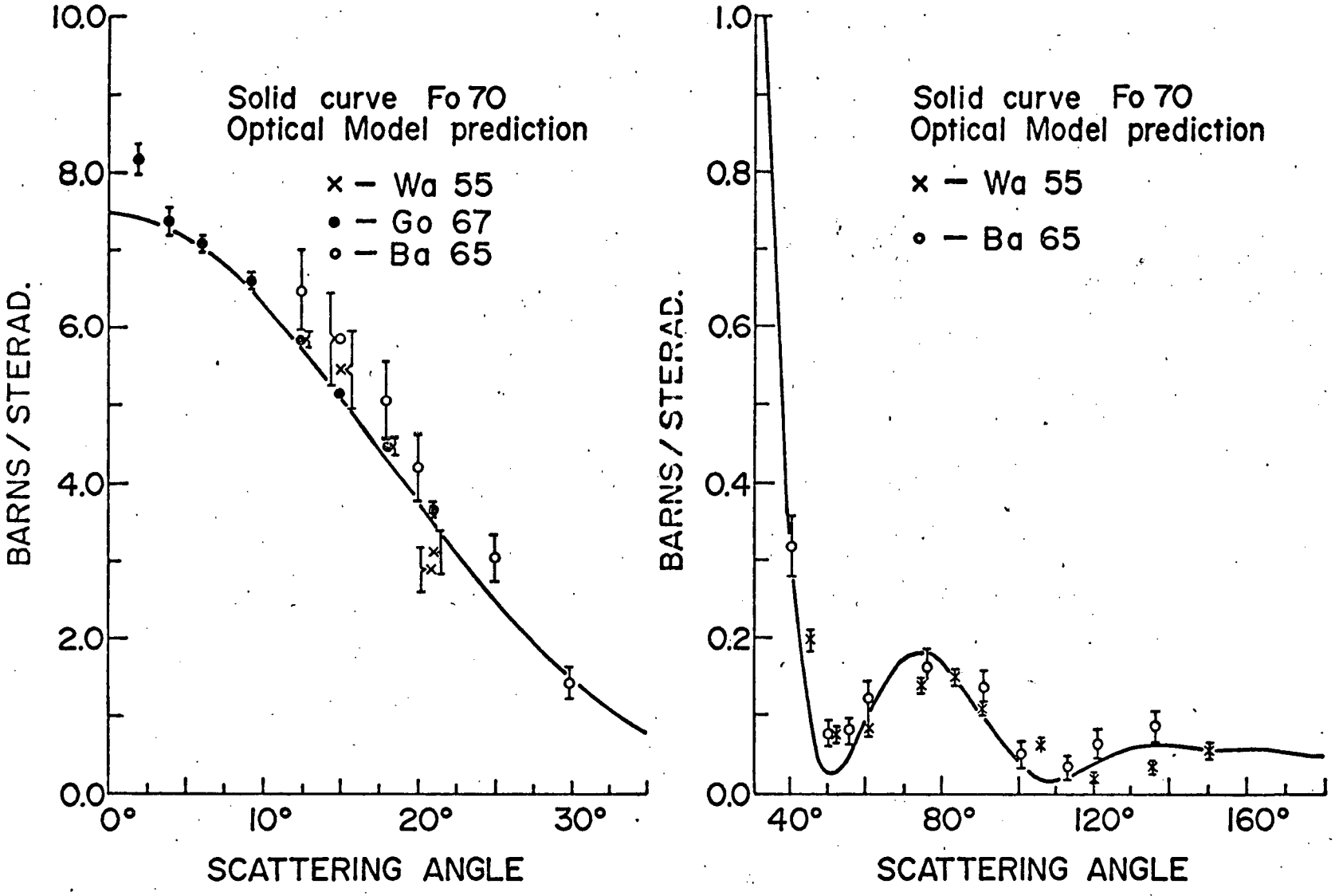

Figure 5-1 Large Angle Optical Model Fit to Previous Experimental Cross Sections. From (Fo 69).

such that

$$V(r) = V_1(r) + V_2(r)$$
$$V_1(r) = 0 \ , \ r \geq r_c$$
$$V_2(r) = 0 \ , \ r \leq r_c \quad ,$$

Here $V_1(r)$ is comprised at both nuclear and electromagnetic terms and $V_2(r)$ contains electromagnetic terms only. Here r_c is a cutoff radius chosen sufficiently large that the short range nuclear forces have fallen to a negligible value. Using a suitable optical model code such as Abacus the phase shifts $\xi_{\ell j}$ may be calculated for the potential $V_1(r)$. The phase shifts for the complete interaction V(r) may be obtained from the $\xi_{\ell j}$ by the relation

$$\tan \delta_{\ell j} = \frac{(1 + b_{\ell j}) \tan \xi_{\ell j} - a_{\ell j}}{1 - b_{\ell j} + c_{\ell j} \tan \xi_{\ell j}}$$

The coefficients a, b, and c are obtained from integral expressions involving the potential $V_2(r)$ and Bessel and Neuman functions. For the electromagnetic interactions with an r^{-3} or r^{-4} radial dependence as in equations (1-9) and (1-13) these expressions are readily integrated. Now, using the usual relationships between phase shifts and the cross sections and polarizations the observables may be calculated (Ho 63).

Forrester has used the parameters of Table 5-1 and the potential of equation (1-4) to calculate the Abacus phase shifts. These were used with the computer program Polecat (El 64) to obtain the cross sections for the scattering of 4.3 MeV neutrons with P_o = -15.4% from lead, bismuth, and uranium. The uranium results are shown in figure 5-2. The calculations were checked using the Schwinger approximation

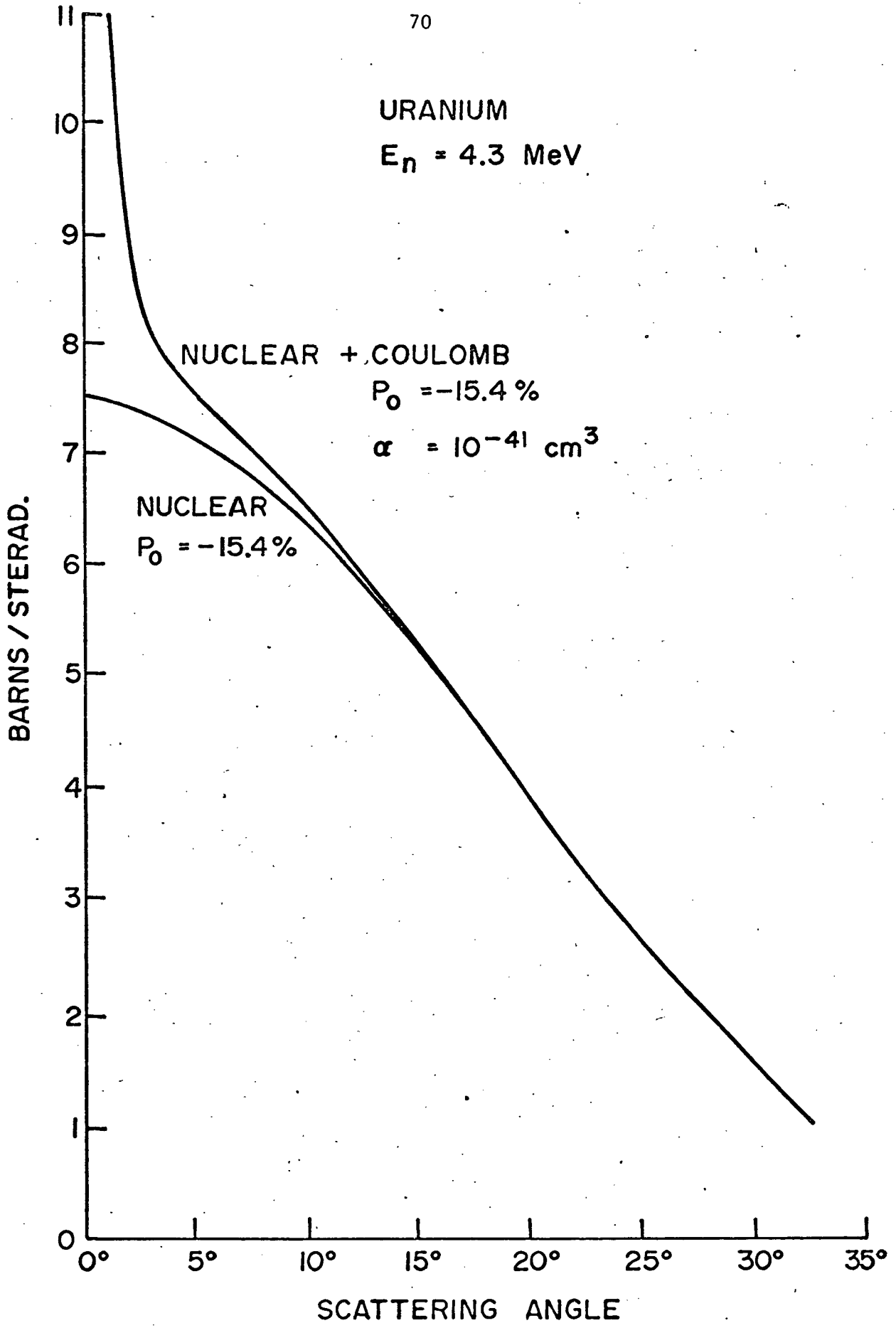

Figure 5-2 Calculated Optical Model Neutron Scattering Cross Sections for Uranium

which showed no significant diviations for the present case.

The effect of including a neutron polarizability as large as $\alpha = 10^{-41}$ cm^3 had no effect on the shape of the angular distribution and only increased the magnitude of the small angle cross section 1%. Thus the statistical accuracy of neutron scattering experiments limits sensitivity to this effect.

As seen in figure 5-2, however, the Schwinger effect is 0.0% at 15^o, 6.5% at 5^o, and rapidly rising below 2.5^o. The results for lead and bismuth are similar and appear below with the experimental cross sections.

5.3.1. Corrected Experimental Cross Sections

The experimental cross sections obtained after the application of the corrections discussed above to the data are shown in figure 5-3. Figure 5-4 shows the ratios of the cross sections to the cross section at 15^o for each target nucleus. In each figure the curves are from the calculations of 5.2.2. The lower curves of figure 5-3 are nuclear only cross sections, while the upper curves are nuclear plus electromagnetic interaction. The curves of figure 5-4 represent calculations containing both nuclear and electromagnetic interactions.

For the case of Bismuth only the ratios of the cross sections in figure V-3 have had a second ordinate added on the right with the ratio at 10^o taken as unity. The broken line in the figure here refers to this right hand ordinate. The solid lines refer to the ordinate on the left which takes the ratio of the cross sections at 15^o as unity.

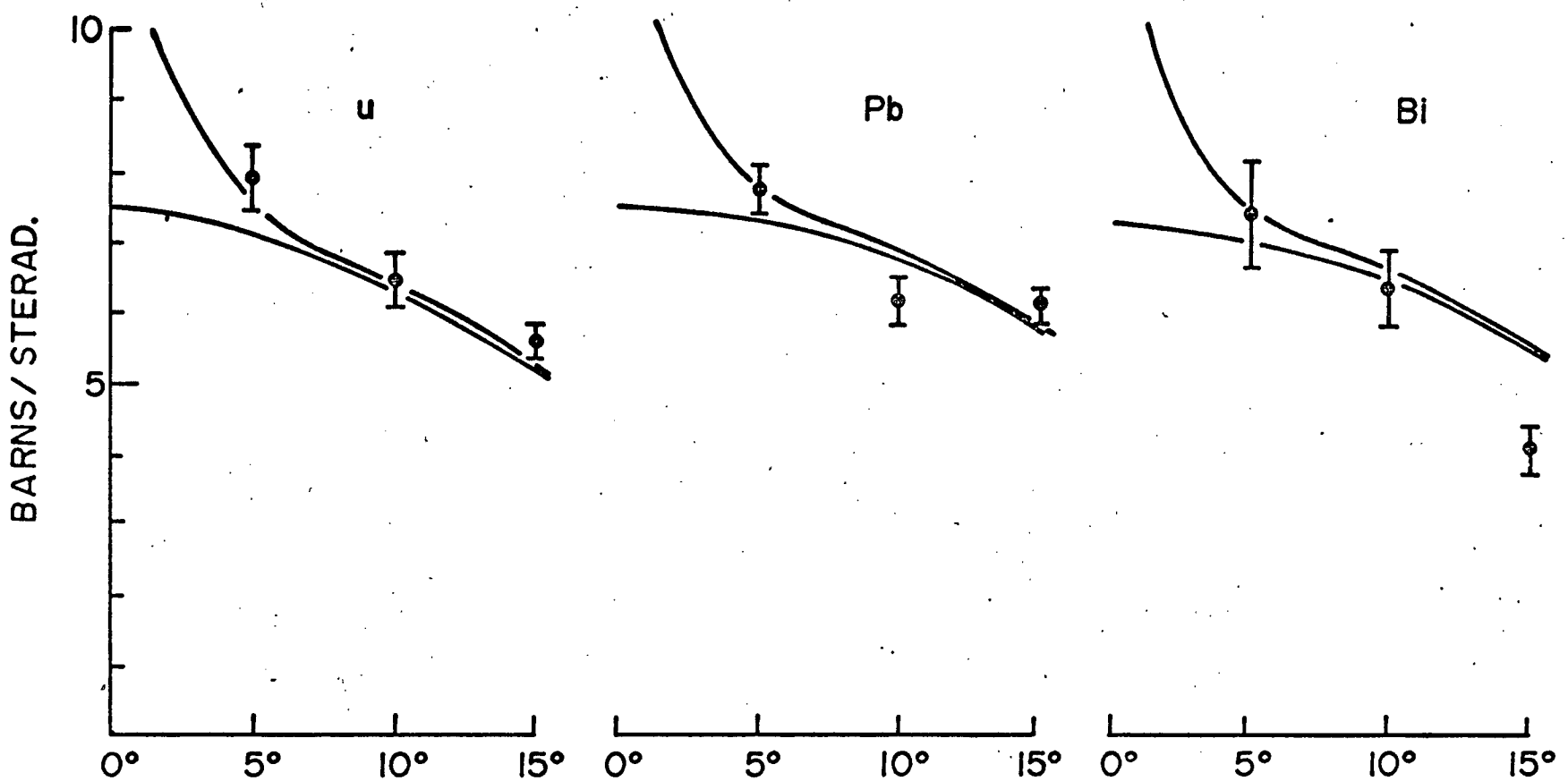

Figure 5-3 Experimental Values of Scattering Cross Sections. Lower Solid Curve Nuclear Only, Upper Solid Cruve Nuclear Plus Schwinger Interactions.

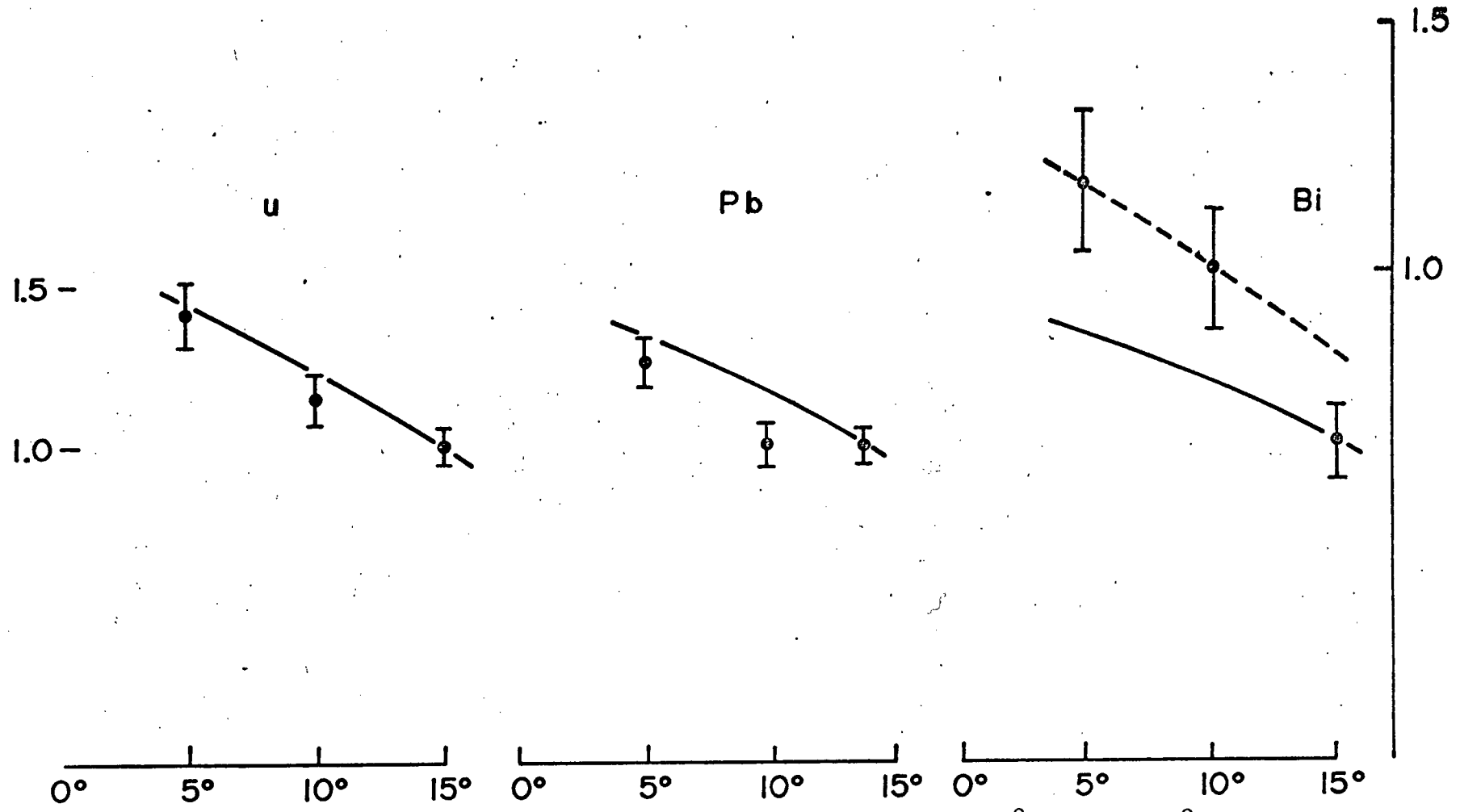

Figure 5-4 Experimental and Calculated Values of $\frac{d\sigma(5^{o})}{d\Omega} \Big/ \frac{d\sigma(15^{o})}{d\Omega}$

See Text for discussion of curves.

The experimental cross sections with corrections of figure 5-3 are shown with statistical errors. Good relative consistency is exhibited with the exception of the 15^{o} measurement for Bismuth. This point is in disagreement with previous measurements (Wa 55) (Go 67) and with the optical model calculations of Chapter 5 (which were based on these measurements). Furthermore, reference to the right hand ordinate and to the broken curve of figure 5-4 shows that the experimental ratio of cross sections for Bismuth at 5^{o} and 10^{o} is in agreement with the value calculated.

In the measurement of the absolute values of the cross sections the uncertainty was ± 9.%. The data of figure 5-3 are presented with relative errors (e.g. ± 5% for uranium at 5^{o}). The same scale is used for the data as for the calculated cross sections, i.e., no scale factors were employed to bring the two into agreement.

5.3.2. Conclusions

On the basis of the present study several conclusions may be drawn. First, there is no evidence that the angular variation of the 4.3 MeV neutron elastic scattering cross sections for uranium, lead, and bismuth are inconsistent with those of calculations involving an optical model interaction and a Schwinger interaction (Ma 73). This is in agreement with the data of Gorlov (Go 67) at 4.0 MeV and of Alexandrov (Al 57) at 3-4 MeV. However, the trend of the present data is not in agreement with the results of Anikin (An 71) (Pe 66) at 4.5 MeV who shows an anomalous increase of 6% at an angle of 5^{o} for uranium and an anomalous increase of

5% at 5^{o} for lead. These results were obtained at neighboring energies. It should be noted that the anomalous behavior of the cross section reported elsewhere (see Chapter 1.3.) may be energy dependent.

Second, the absolute value of the experimental cross sections of the present work are in agreement with those calculated with an optical model potential obtained from a fit to previously published data plus a Schwinger interaction. The data for the fitted optical model potential parameters were from the energy range 4.0 to 4.4 MeV and for angles greater than 15^{o}. Other workers, for example Kuchnir et. al. (Ku 68) using the average parameters of Auerbach and Moore (Au 64), have found discrepancies between calculated and experimental absolute values of the cross sections. Furthermore, the present work is in agreement with the absolute values of the cross sections for lead and uranium at forward angles in the range 2^{o} to 20^{o} obtained previously by Gorlov at 4.0 MeV. This is in clear disagreement with the data of Anikin (An 71) for lead (only) which shows a discrepancy of 18%, the cross sections being low. Since the absolute cross sections of Anikin for uranium at forward angles are in agreement with those of the present work and those of Gorlov, we see evidence for an internal inconsistency in the experimental cross sections of Anikin.

Third, from an experimental standpoint, a basis has been established for the viability of the associated particle technique in small angle scattering experiments. Major improvements over previous work (Tr 67) using the $D(d,n)^{3}He$ reaction as the source of tagged neutrons have been attained: the development of thin rotating targets (McF 73) with target lifetimes of 2×10^{5} microcoulombs for incident 2 MeV deuterons has been

accomplished; typical target yields corresponded to 15 μgm cm^{-2} equivalent of deuterated polyethylene resulting in a neutron beam intensity of 81 m sec^{-1} $msterad^{-1}$ at a deuteron beam current of 1.2 μa; the use of a position sensitive detector in fast timing applications has been demonstrated (McF 71) in conjunction with a multiparameter ADC - mini-computer system for on-line data logging and preliminary analysis. By the use of extensive room shielding, a neutron beam collimator, and neutron-gamma ray pulse shape discrimination, a signal to background ratio (i.e. sample in/sample out) of 4:1 was obtained at 5^{o}, and a ratio of 9:1 at 15^{o}. The associated particle technique as developed in the present work has been shown to provide adequate collimation of a neutron beam for a minimum scattering angle of 3^{o}. Possible improvements in this performance are discussed below.

5.4. Suggested Future Experimental Improvements

To pursue further neutron scattering experiments with the associated particle technique several experimental developments should be undertaken. An incident neutron beam of greater intensity would be desirable. The neutron counting rates achieved in the experiment were severely limited by the average current of 1.2 microamperes available on target from the University of British Columbia Van de Graaff machine.

Using the rotating target system described above, a program of optimization of the deuterated polyethylene target construction along the lines of Makovsky and Hojvat (Ma 69) should be undertaken. It should prove possible to improve the yield of scattered neutrons in this way

without sacrificing fast timing resolution and neutron beam width to an unacceptable degree.

The incorporation of a neutron detector hodoscope would also be advantageous for performing the angular distribution measurements. Care must be exercised here to avoid spurious events such as $(n,n'\gamma)$ reactions between the hodoscope elements themselves.

An important area for development work lies in the optimal design of the neutron beam collimation.

The incorporation of a superconducting neutron spin precession solenoid would be desirable for polarization studies.

APPENDIX 1

Neutron Detector Efficiency Calculation

The neutron detector efficiencies were calculated using a computer program due to Grandy (Gr 67). Using this program and an associated particle neutron beam Heggie (He 72) has found excellent agreement between the theoretical calculations and measured efficiencies for a 5 inch diameter x 3 inch deep NE218 cylinder at neutron energies in the range 2.1 to 2.86 MeV.

The theoretical efficiency calculation accounts for single and double neutron-proton scattering and single neutron-carbon scattering. An infinite area detector is assumed. This assumption is supported by two properties of neutron-proton scattering. First the laboratory differential cross section decreases as the cosine of the neutron scattering angle. Second, the energy of the scattered neutron decreases as the square of the cosine of the neutron scattering angle. The relatively low probability of a neutron scattering through a large angle is associated with a low energy and hence a short mean free path. Thus there is little "leakage" of neutrons from the sides of a finite detector and correspondingly the calculated efficiency is not expected to be significantly over estimated.

The computer program uses the hydrogen and carbon neutron scattering cross sections, a kinematical expression, and an integration over the detector volume to obtain the expected proton recoil spectrum. However the photomultiplier output for a monoergic group of protons has a

distribution which may be approximated by a gaussian. This arises from the statistical natures of the light pulse and the photoelectrons in the photomultiplier which contain a finite number of particles. A gaussian is folded with the proton recoil spectrum in order to account for this effect in the photomultiplier output. The efficiency is then obtained by an integration over the photomultiplier output which includes the lower level discriminator setting.

The computation used a neutron lower level TSCA discriminator setting of 0.26 MeV. This setting was obtained experimentally from the ^{241}Am 60. keV gamma ray. Batchelor (BA 61) has investigated the electron proton equivalent relationship, and his equations for NE213 have been applied:

$$E_e = 0.215\ E_p + 0.028\ E_p^2 \qquad 0 < E_p < 8 \text{ MeV}$$

$$E_e = 0.60\ E_p - 1.28$$

The calculated efficiency of the 2.76 inch deep NE218 scintillator was 37 %, that of the 4 inch deep was scintillator 44 %.

APPENDIX 2

Neutron Multiple Scattering

In a neutron scattering sample of finite thickness a neutron may scatter sequentially from more than one target nucleus before leaving the scattering sample. This process of neutron multiple scattering is important since the shape of the observed angular distribution of scattered neutrons can be significantly altered by an averaging over angles. Knowledge of the nuclear scattering process is inferred from the angular distribution and hence multiple scattering effects reduce the information contained in the experimental data.

In order to obtain acceptable count rates it is frequently necessary to employ scattering samples of thickness corresponding to a sizable fraction of a neutron mean free path. Furthermore, to a certain extent the effects of neutron multiple scattering may be calculated and corrected for in the data. In the practical case this is what is done; data is taken with samples of reasonable thickness and multiple scattering effects are estimated by calculation.

In the calculation of the effects of neutron multiple scattering Monte Carlo techniques (Co 67), analytical techniques (Ku 70), and combinations of both of these (Co 67) have been used. Probably the most widely employed has been the Monte Carlo method.

In this instance a digital computer program is devised to simulate the experiment and neutron histories are traced, one by one, from the neutron beam into the scattering sample, and thence to the neutron

detectors. In the program, for each artificial neutron scattering, the angles of emission of the outgoing neutron are chosen at random and the angular variation of the scattering intensity is weighted by an assumed neutron angular distribution. The neutrons thus perform a sort of random walk through the apparatus. The computer program tabulates the number of neutrons recorded at each angle and classifies them as to the order of scattering, i.e., once, twice, ... k scattered. Once a statistically significant number of neutron scattering "events" have been followed, the program output gives the calculated or simulated angular distribution to be expected in an experiment. Angular distributions for the different orders of scattering and their relative intensities are also available.

The Monte Carlo technique is subject to the limitations of statistical accuracy and initial conditions. Essentially both these restrictions stem from computing time restrictions. The time required to run a program is proportional to the number of neutron histories traced. The average length of time necessary to examine a neutron history is increased with each initial boundary condition considered. As a result it is common practice, for example, to limit the incident neutron beam profile to a delta function.

One more possible defect of Monte Carlo calculations lies in the quality of the random number generators used. Recently some of the methods of obtaining a sequence of random numbers have been called into question.

An alternative approach to the calculation of multiple scattering effects lies in an analytical method (Ku 70) applicable to scattering samples possessing cylindrical geometry and dimensions of the order of

one neutron mean free path or smaller. For this case, the third order scattering is not an important effect and it is possible to neglect it a priori. In any event it is possible to test this assumption. In the present work this analytical method has been used.

A beam of neutrons is incident upon the end face of a scattering sample in the form of a right circular cylinder and scattered neutrons are detected at an angle θ as shown in figure A-2-1. It is necessary to find the calculated count rate $dR_1(\theta)$ of once (and once only) scattered neutrons due to an element of volume dV of the scattering sample. Make the following definitions:

N_0 = incident neutron beam intensity

$f(xyz)$ = " " " " distribution

g_1, g_2 = attenuation coefficients for neutrons in the sample before and after scattering respectively

$\sigma(E^*,\theta)$ = Cross section for scattering from level E^*

$\varepsilon(E)$ = neutron detector efficiency at energy E

Ω = " " solid angle

N = density of scatterer

E_0 = neutron incident energy

Then the count rate $dR_1(\theta)$ is:

(A-2-1) $$dR_1(\theta) = N_0 f(xyz) g_1 \sigma(E^*,\theta) \varepsilon(E) g_2 \Omega N dV$$

In order to facilitate integration over the sample volume we make the approximation that the variations of θ, Ω, and E over the sample volume are not important and if necessary a correction separate from the multiple scattering calculation may be made to the data. We then obtain:

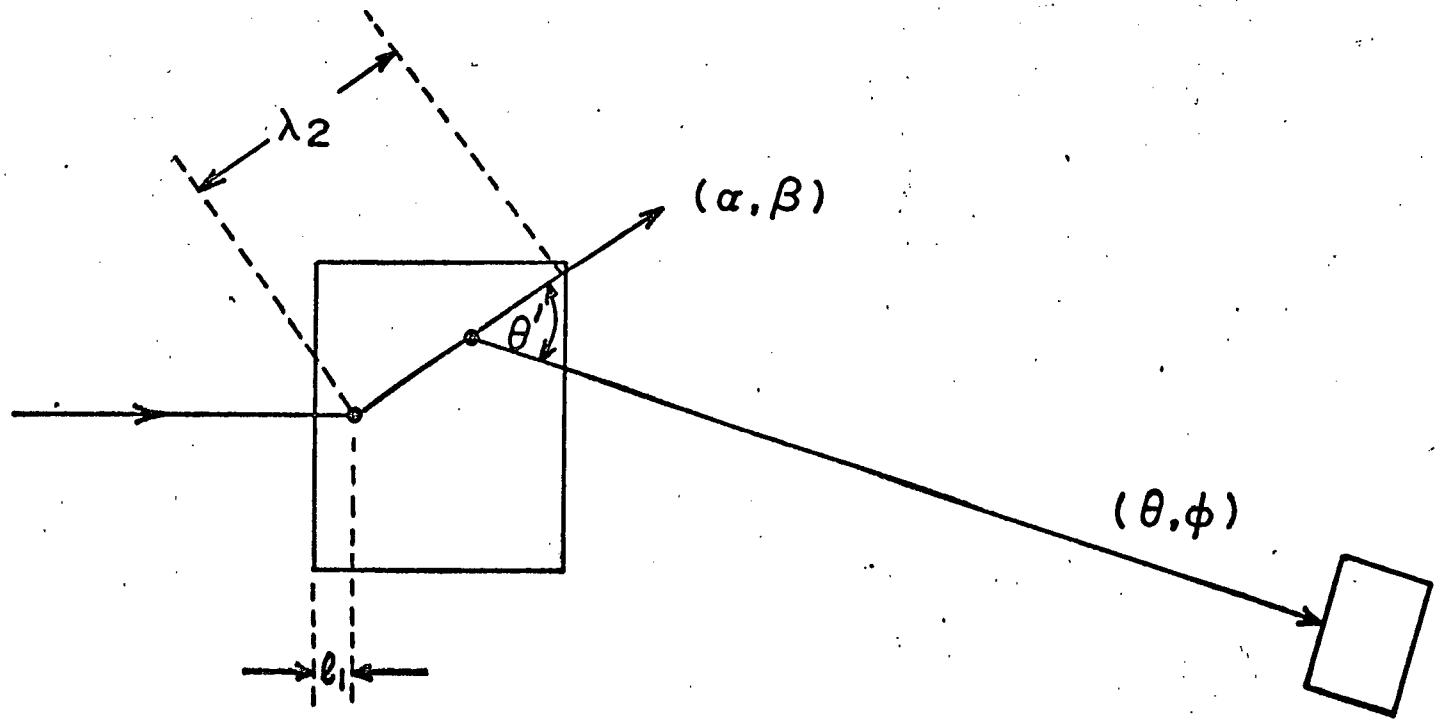

Figure A-2-1 Sample-Neutron Detector Geometry

(A-2-2) $R_1(\theta) = \int dR_1(\theta) = N_0 N \varepsilon(E_1)\Omega\sigma(E^*,\theta) \int dV f(xyz) g_1 g_2$

In order to account for the possibility of using inelastic processes in the calculation, $\varepsilon(E_1)$ denotes the detection efficiency for a neutron whose energy has been changed by the first collision. The g_i are obtained from the macroscopic total cross sections Σ_i by:

(A-2-3) $g_i = \exp(-\Sigma_i \ell_i)$ $\qquad i = 1$ or 2

Here ℓ_i is the neutron path length in the scattering sample before and after interaction respectively, as shown in figure A-2-1. For convenience we write $S_{x\cdot n}(\theta)$ to be the angular distribution of scattered neutrons per incident neutron, per target nucleus, per unit solid angle. The angular distribution is subscripted:

$x = E$ or I $\qquad$ internal, or external to sample

$n = 1$ or 2 $\qquad$ order of scattering

Then:

(A-2-4) $S_{x\cdot n} = R(\theta) / A$ $\qquad$ with: $A = N_0 N \varepsilon(E_1)\Omega.$

From equation (A-2-2) the angular distribution of once scattered neutrons outside the sample is:

(A-2-5) $S_{E\cdot 1}(\theta) = \sigma(E^*,\theta) \int dV f(xyz) g_1 g_2$

By dropping the attenuation of the outgoing neutrons we obtain the internal angular distribution of once scattered neutrons:

(A-2-6) $S_{I\cdot 1}(\theta) = \sigma(E^*,\theta) \int dV f(xyz) g_1$

This internal angular distribution has a probability of escape from the sample of g_2, with a probability of interaction $(1 - g_2)$. But, this accounts for all processes and must be weighted by the fraction of

processes that contribute to plural scattering, (Σ_{pl} / Σ_t) to obtain the probability that a neutron will scatter a second time:

$$(A\text{-}2\text{-}7) \quad W(E,\ell_2) = (\Sigma_{pl} / \Sigma_t)\ (1 - \exp(-\Sigma_t\ \ell_2)).$$

Now, inside the scatterer, the neutrons that have scattered once and will scatter once again have the distribution:

$$(A\text{-}2\text{-}8) \quad S_{I\cdot 1\to 2}(\theta) = \sigma(E^*,\theta) \int dV\ f(xyz)\ g_1\ W(E_1,\ell_2).$$

Expand this in the usual Legendre Polynomial series.

$$(A\text{-}2\text{-}9) \quad S_{I\cdot 1\to 2}(\theta) = \sum_n \beta_n\ P_n(\cos\ \theta).$$

We define the following angles:

α = polar angle of first scattering

β = azimuthal " " "

θ' = angle between first and second scattering

ϕ = azimuthal angle of second scattering

θ = polar " " " "

Expanding now the scattering cross section for the second scattering process in another Legendre series, we obtain:

$$(A\text{-}2\text{-}10) \quad \sigma(\theta') = \sum_n \gamma_n\ P_n(\cos\ \theta')$$

Since the angle integrated cross section is just $4\pi\gamma_0$ the angular variation of the probability of second scattering is:

$$P(E_1,\theta') = \sum_n \gamma_n\ P_n(\cos\ \theta') \ /\ 4\ \pi\ \gamma_0\ .$$

The addition theorem for spherical harmonics is now used to relate the functions of two directions (α,β) and (θ,ϕ) separated by an angle θ'.

$$(A\text{-}2\text{-}11) \quad P(E_1,\theta')=P(E_1,\alpha,\beta,\theta,\phi) = \sum_n \gamma_n\ (1/\gamma_0(2n+1)) \sum_{m=-n}^{n} Y_n^m(\alpha,\beta)\ Y_n^m(\theta,\phi)$$

The angular distribution of second scattered neutrons inside the sample can be found now by weighting $S_{I\cdot 1\to 2}(\theta)$ with $P(E_1,\alpha,\beta,\theta,\phi)$ and integrating over angles.

$$(A\text{-}2\text{-}12)\quad S_{I\cdot 2}(\theta) = \iint d\Omega S_{I\cdot 1\to 2}(\theta)\ P(E_1,\alpha,\beta,\theta,\phi)$$

$$= \int_0^{\pi} d\alpha\ \mathrm{Sin}\ \alpha \int_0^{2\pi} d\beta \sum_k \beta_k\ P_k(\cos\alpha) \sum_n \sum_{m=-n}^{n} (\gamma_n/\gamma_0(2n+1))\ x$$

$$Y_n^m(\theta,\phi)\ Y_n^m(\alpha,\beta)$$

By use of the definition of the Legendre Polynomials in terms of the spherical harmonics and by use of the orthogonality relationship for spherical harmonics, this integration yields:

$$(A\text{-}2\text{-}13)\quad S_{I\cdot 2}(\theta) = \sum_k \beta_k\ (\gamma_k\ /\ \gamma_0\ (2k+1))\ P_k(\cos\theta)\ .$$

But from the condition that the sample is of the order of one neutron mean free path and the consequent negligibility of third order scatterings with respect to first order, this internal distribution suffers no attenuation. So:

$$(A\text{-}2\text{-}14)\quad S_{E\cdot 2}(\theta) = S_{I\cdot 2}(\theta)$$

and:

$$R_2(\theta) = S_{E\cdot 2}(\theta)\ (N_0\ N\ \varepsilon(E_2)\ \Omega)\ .$$

Again E_2 allows for an inelastic process at the second scattering. The total calculated count rate is:

$$(A\text{-}2\text{-}15)\quad R(\theta) = R_1(\theta) + R_2(\theta)$$

In a study of neutron multiple scattering Cox (Co 67) compared the results of Monte Carlo and analytical formalisms. Several important

conclusions were drawn for scattering samples with dimensions of approximately one mean free path. First, define the ratios

(A-2-16) $R_{21} = (2) / (1)$ and $R_{31} = (3) / (1)$

where (1), (2), etc. are the angle integrated intensities of first, second, etc. order scattered neutrons. Then these quantities are related by:

(A-2-17) $$R_{31} = (R_{21})^2 / (1-R_{21})$$

These ratios are not strongly affected by the shape of the angular distributions. For sample thicknesses up to one half of a mean free path they are independent of the shape to one percent accuracy or better. In the range of thickness one half to one mean free path, R_{21} for a strongly forward peaked angular distribution of neutrons, is about 5% higher than for an isotropic distribution. This implies that R_{21} may be used with confidence for any realistic distribution to predict the ratio R_{31}. Remember, it is only important to establish that R_{31} is small and of the order of the experimental errors. Also, $R_{31} = (R_{21})^2 / (1-R_{21})$ over estimates the contribution of third order scattering in the region from one half to one mean free path by about 5%. Again, this is unimportant in establishing that third order scattering is negligible.

From the analytical formalism developed above:

(A-2-18) $$(1) = \int d\Omega \, S_{E\cdot 1}(\theta)$$

$$(2) = \int d\Omega \, S_{I\cdot 1\to 2}(\theta) = 4\pi\beta_0 \quad .$$

The contribution of third order scattering can then be obtained by

equations (A-2-16) and (A-2-17).

Using a computer program the effects of multiple scattering as a function of sample thickness were studied. The case chosen as representative was 4.25 MeV unpolarized neutrons incident on lead. The angular distribution is that of figure A-2-2 (Fo 69). Only nuclear elastic processes were considered. For lead the total neutron cross section is σ_t = 7.68 barns, the density, 3.30 x 10^{22} cm.$^{-3}$ and hence a neutron mean free path of λ = 3.95 cm. Calculations were done for sample thicknesses t = 1,2,3, and 4 cm., with a sample diameter of 3.18 cm.

Figures A-2-3 to 6 show the calculated angular distributions of first and second order scattering. In each the top line is the program input. The ratios of second and third order scattering to first order are shown in figure A-2-7a as a function of sample thickness.

It is apparent that R_{21} increases linearly with t, the sample thickness, while R_{31} increases at about $t^{2.5}$. Note that it is above t = 2 cm. that the third order scattering increases rapidly and becomes a significant fraction for second order scattering, the two becoming equal at t = 3.5 cm. Since the calculation of second order scattering was based upon the neglect of third order, this implies that above t = 2 cm. the analytical method is beginning to fail for the present geometry.

Because third order scattering is averaged out by three interactions its angular distribution is nearly isotropic over 2 π. An estimate of the systematic error introduced into $S_{E\cdot 1}(15^o)$ and $S_{E\cdot 2}(15^o)$ by third order scattering is shown in figure A-2-7b as a function of sample thickness. Also included for comparison is the effect of second order scattering

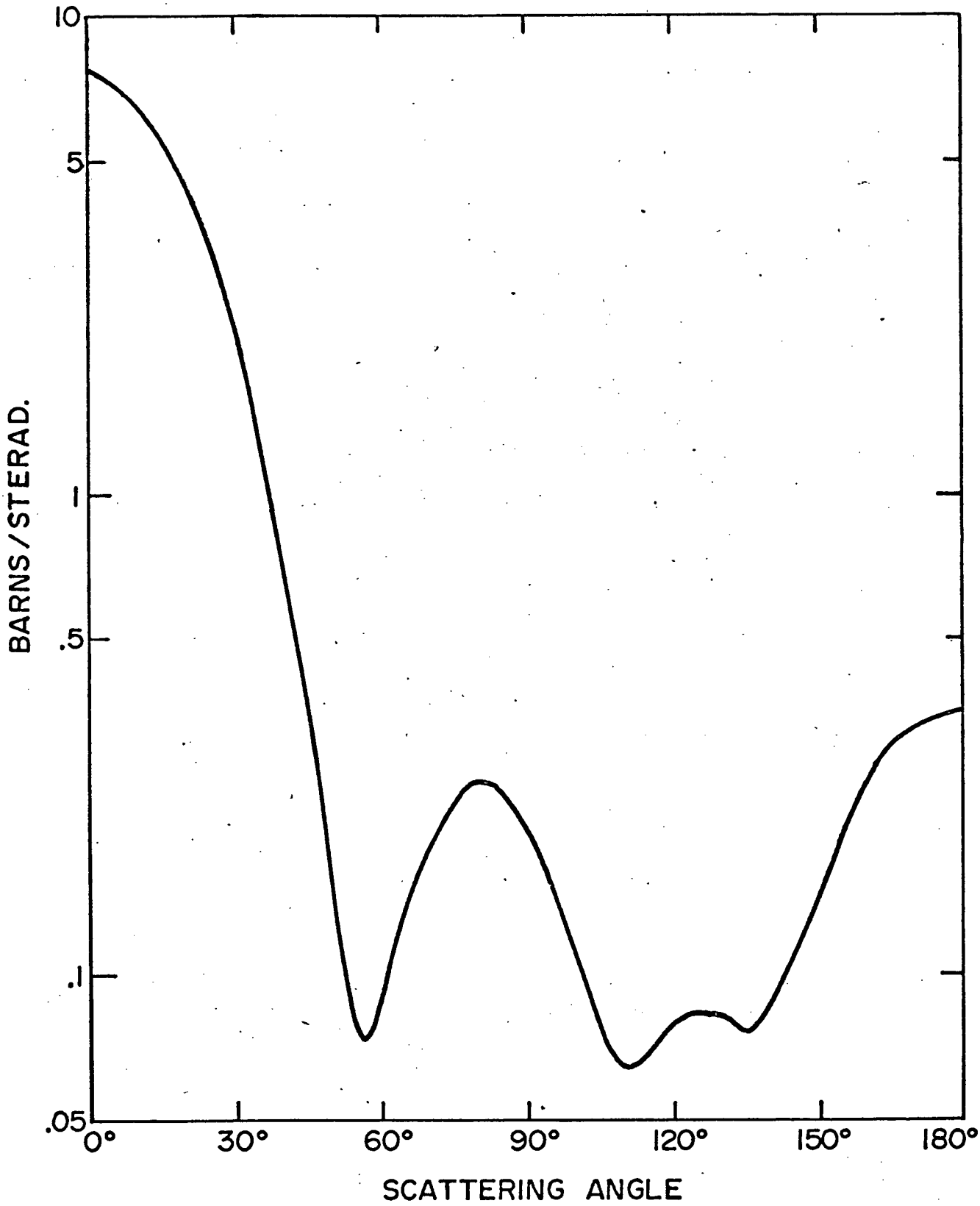

Figure A-2-2 Neutron-Lead Differential Elastic Cross at 4.3 MeV

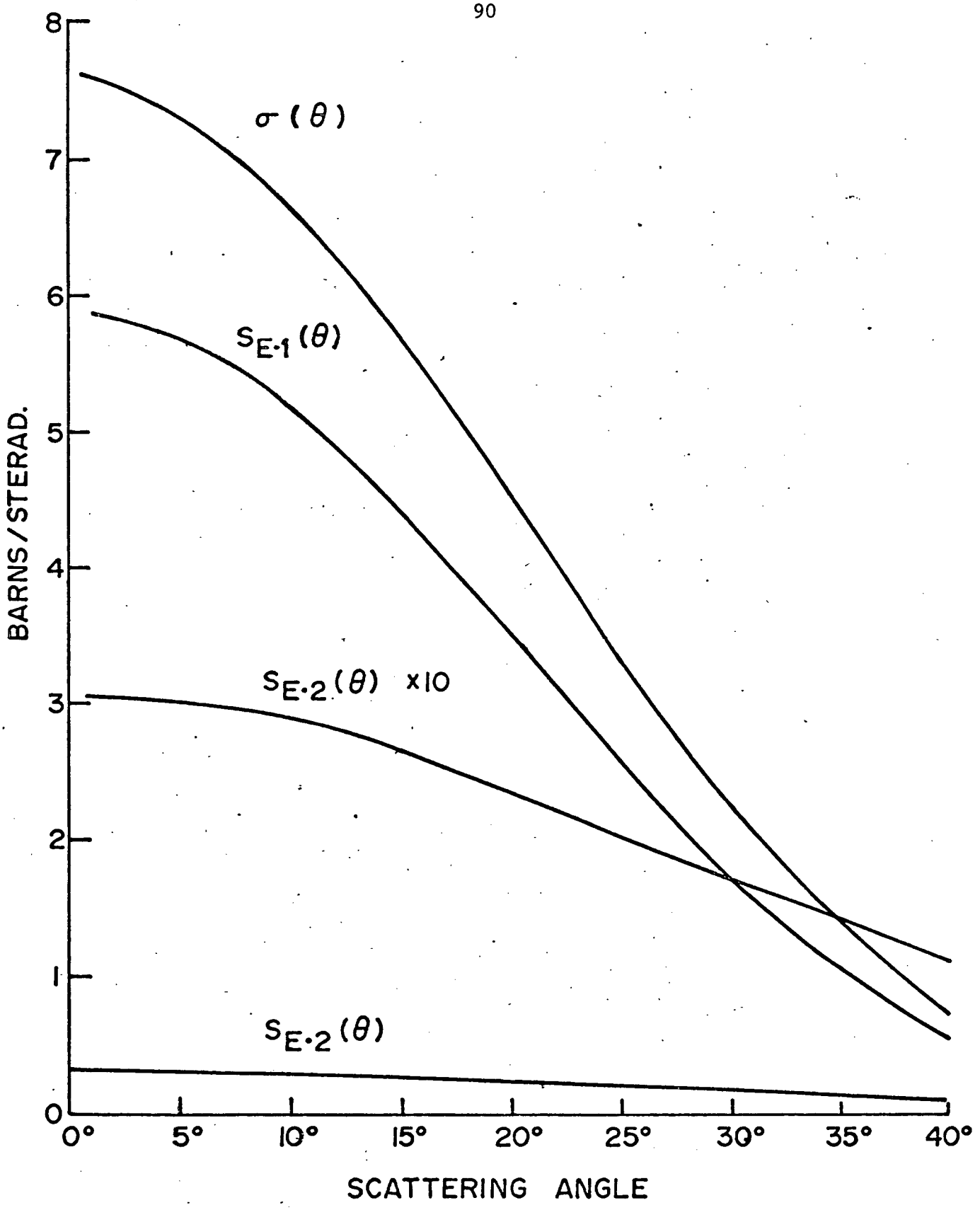

Figure A-2-3 Lead 1 cm. Elastic Elastic Multiple Scattering

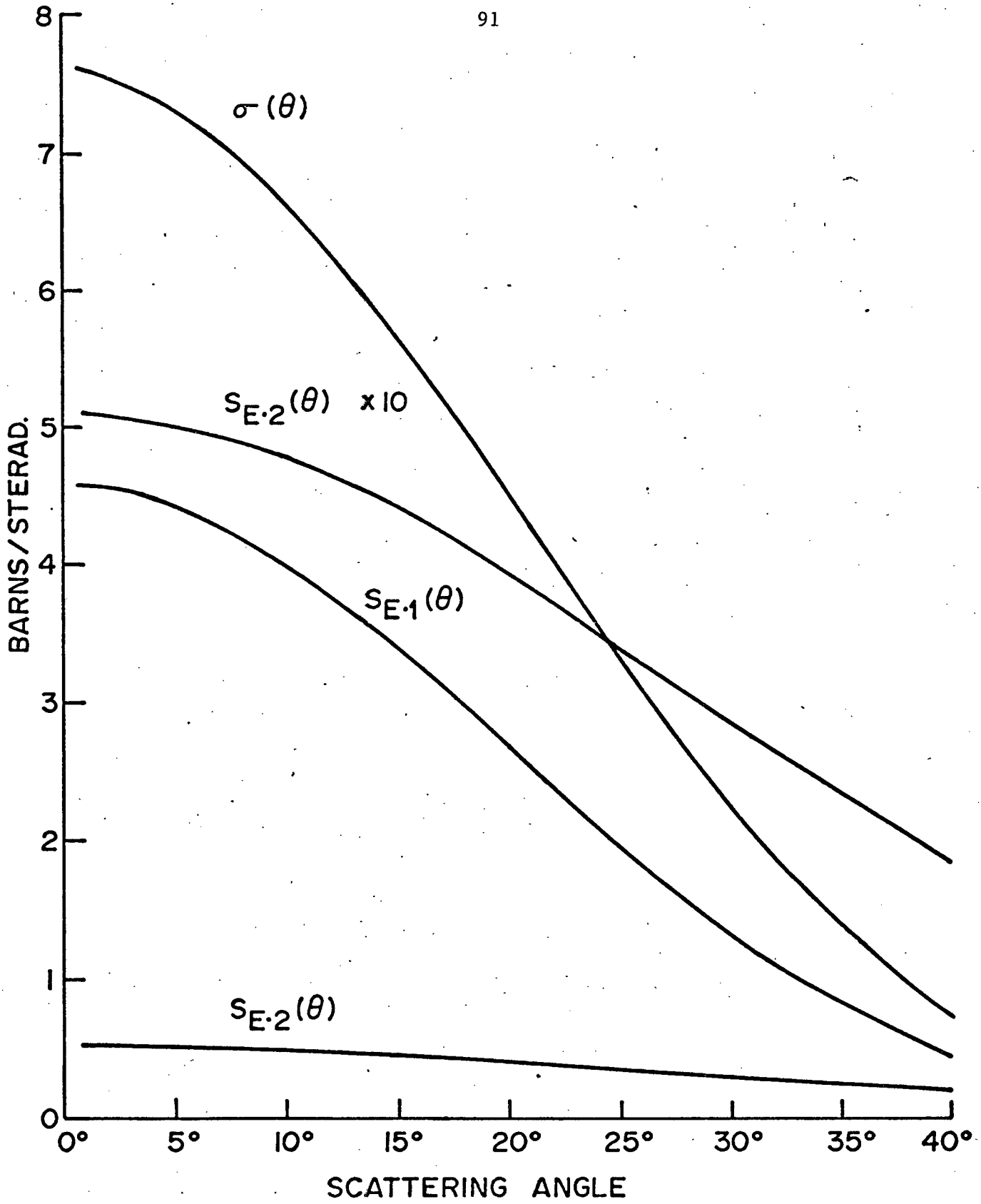

Figure A-2-4 Lead 2 cm. Elastic Elastic Multiple Scattering

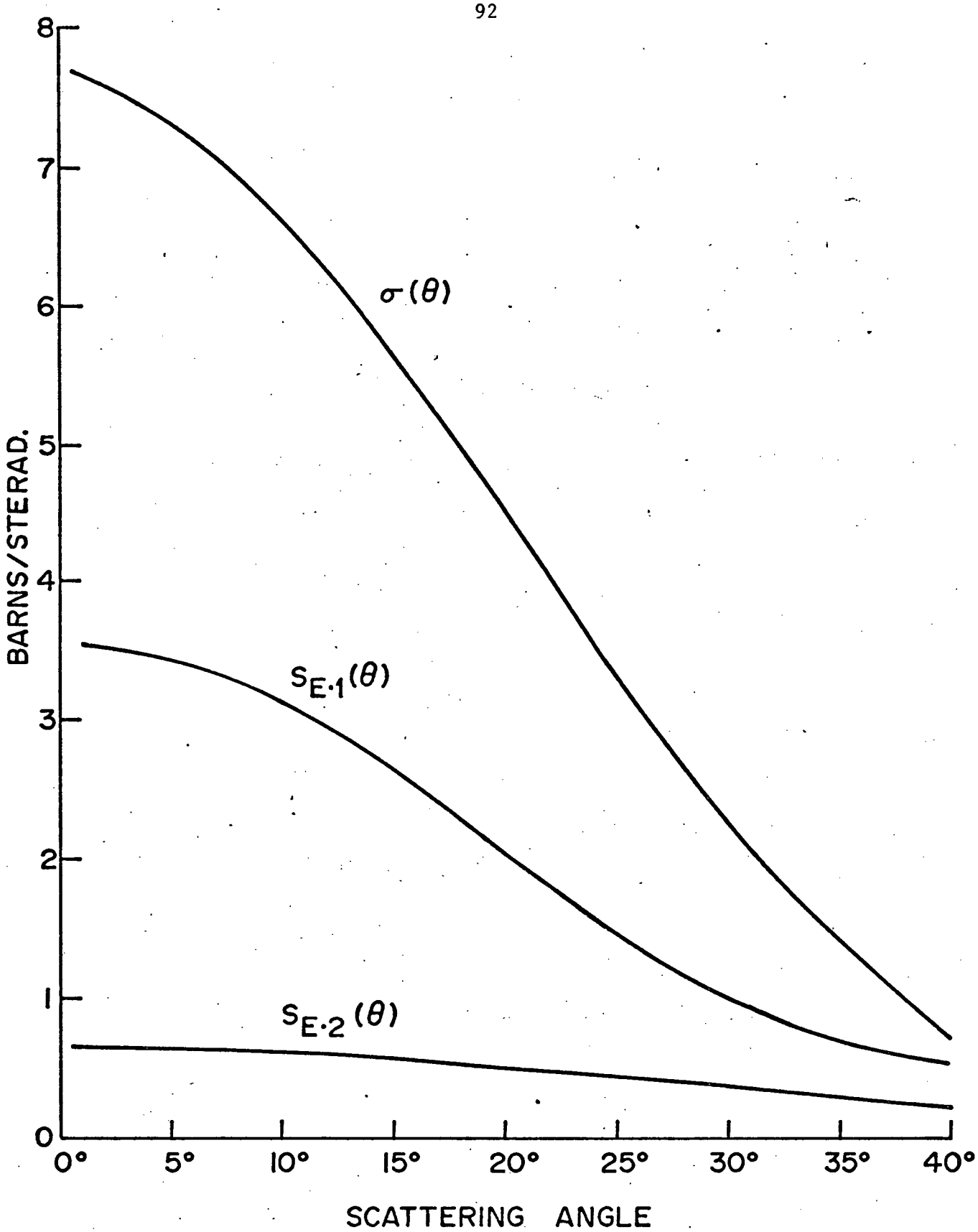

Figure A-2-5 Lead 3 cm. Elastic Elastic Multiple Scattering

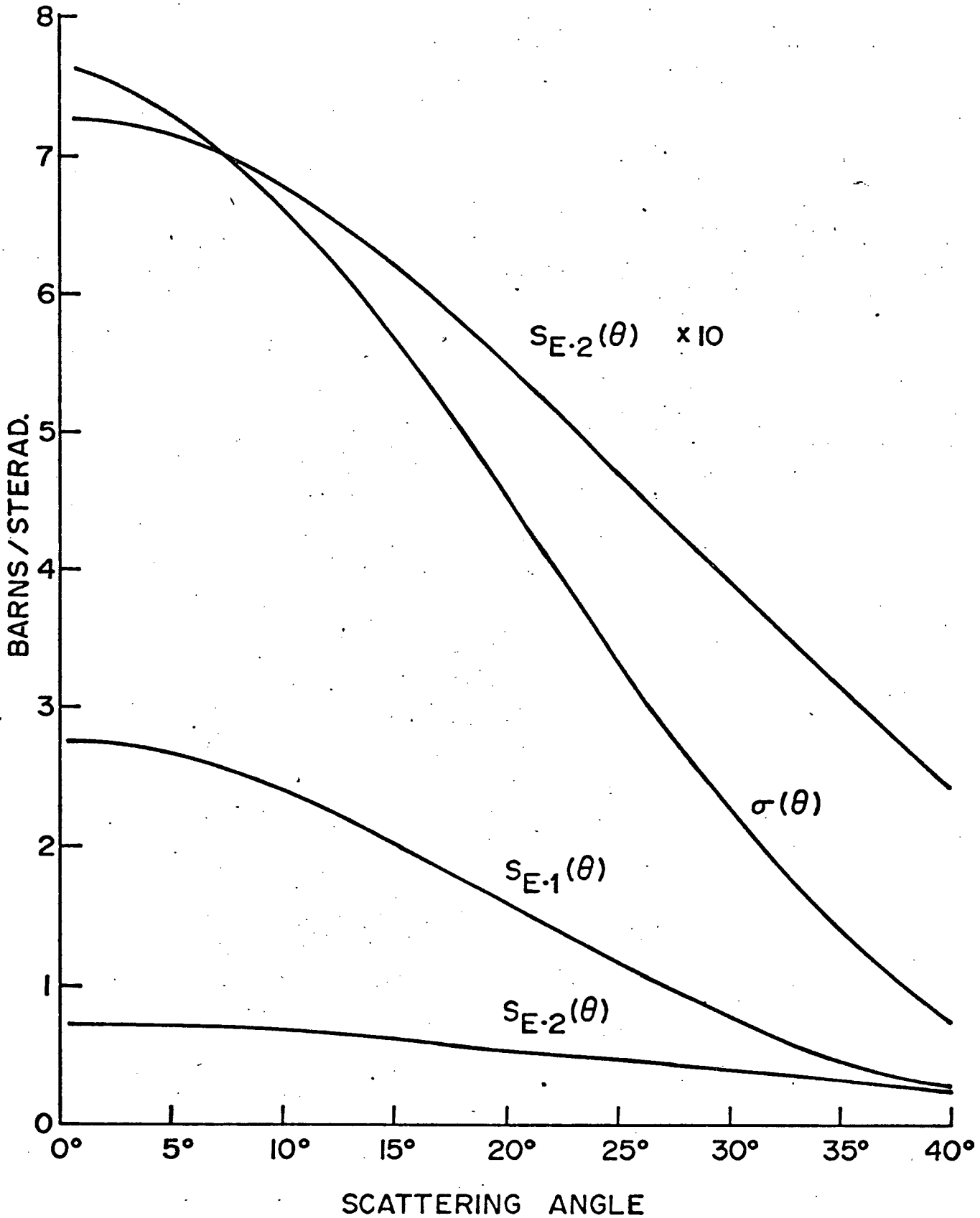

Figure A-2-6 Lead 4 cm. Elastic Elastic Multiple Scattering

on first order scattering. This makes it possible to see explicitly the effects of third order scattering on the differential cross section which would be measured in an experiment. The conclusion that may be drawn is that above t = 2 cm. the effects of third order scattering become important because the percentage of the differential cross section it represents is approximately the same as the statistical accuracy that would be sought in an experiment.

The calculated count rate at a scattering angle of 5^{o} of once scattered neutrons is shown in figure A-2-8 as a function of sample thickness. On the left hand ordinate is the count rate $r = (S_{E\cdot 1}(5^{o}))\ (t)$ in arbitrary units. On the right hand ordinate is the quantity $\sqrt{r}\ /\ \sqrt{r}_{T=1cm.}$. This indicates the improvement in statistical accuracy achieved in a fixed counting time experiment as the sample thickness is increased. The straight line is the product $\frac{d\sigma}{d\Omega}\ t$ or the count rate that would be expected if no attenuation of the neutron beam or scattered neutrons took place. It may be seen that above approximately 1 cm. sample thickness the counting rate is beginning to be dominated by multiple scattering effects and not sample thickness. For example, if experimental time were to be spent obtaining 5% statistical accuracy with a 1 cm. sample, the same time spent with a 2 cm. sample would improve the accuracy to only 4%, and a 3 cm. sample to 3.7%. Note also that there is a maximum count rate at about $t = \lambda$.

From the above figures it may be inferred that an acceptable choice of sample thickness for a neutron scattering experiment would be t = 1 cm. This achieves a trade off between (a) obtaining most of the count rate or statistical accuracy available from sample thickness and

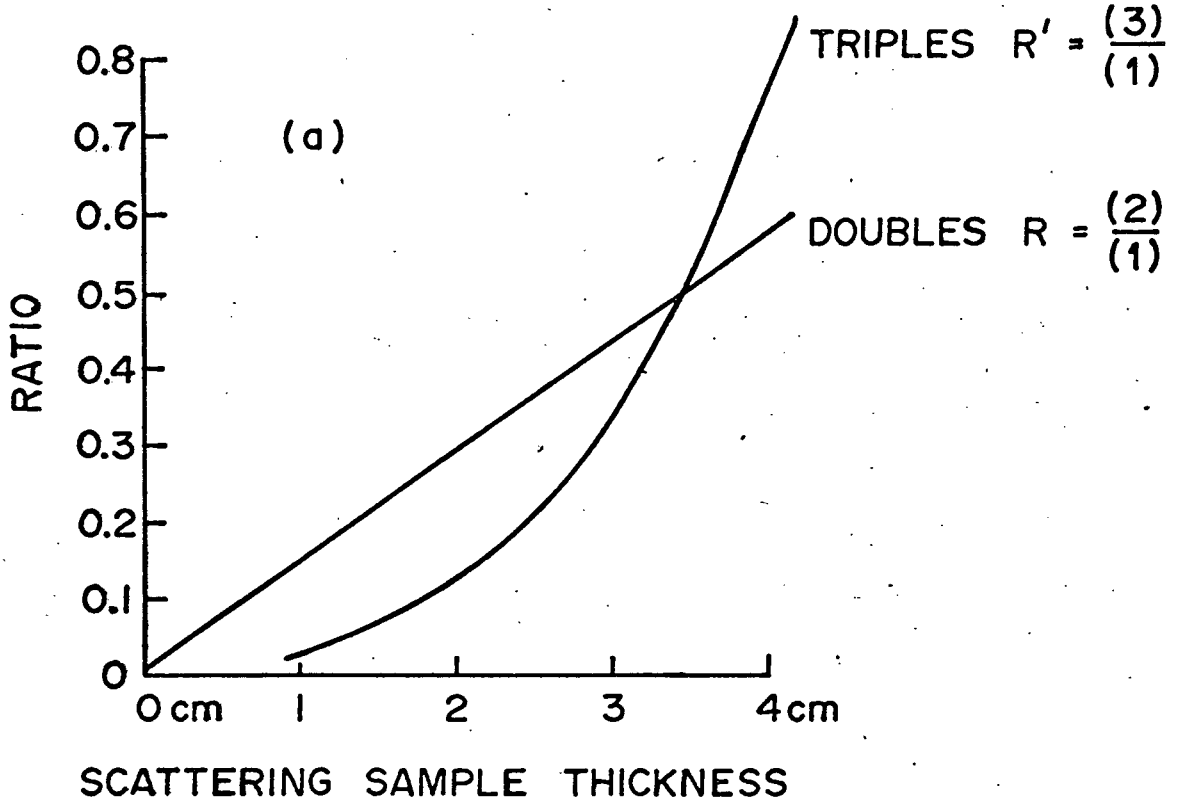

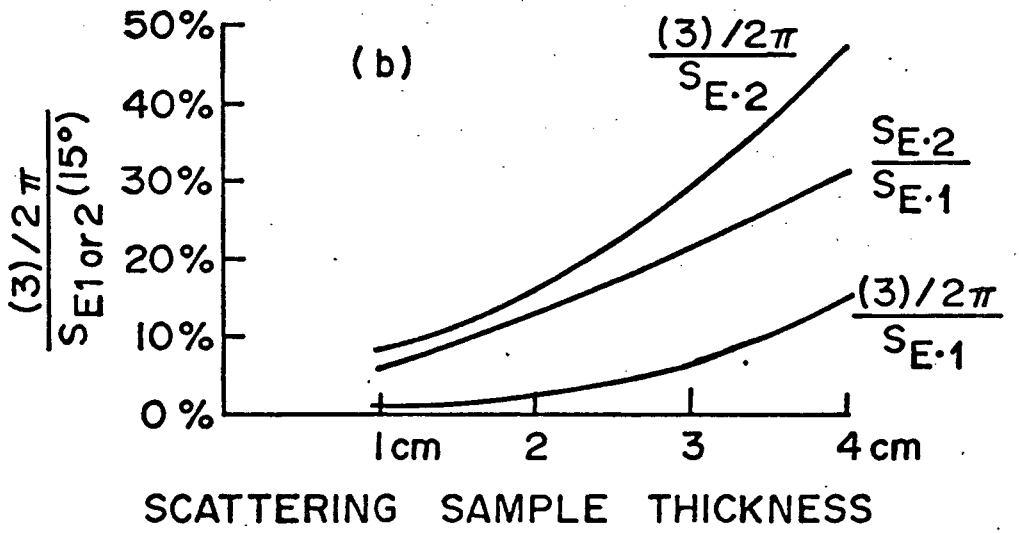

Figure A-2-7 Double and Triple Multiple Scattering vs. Sample Thickness

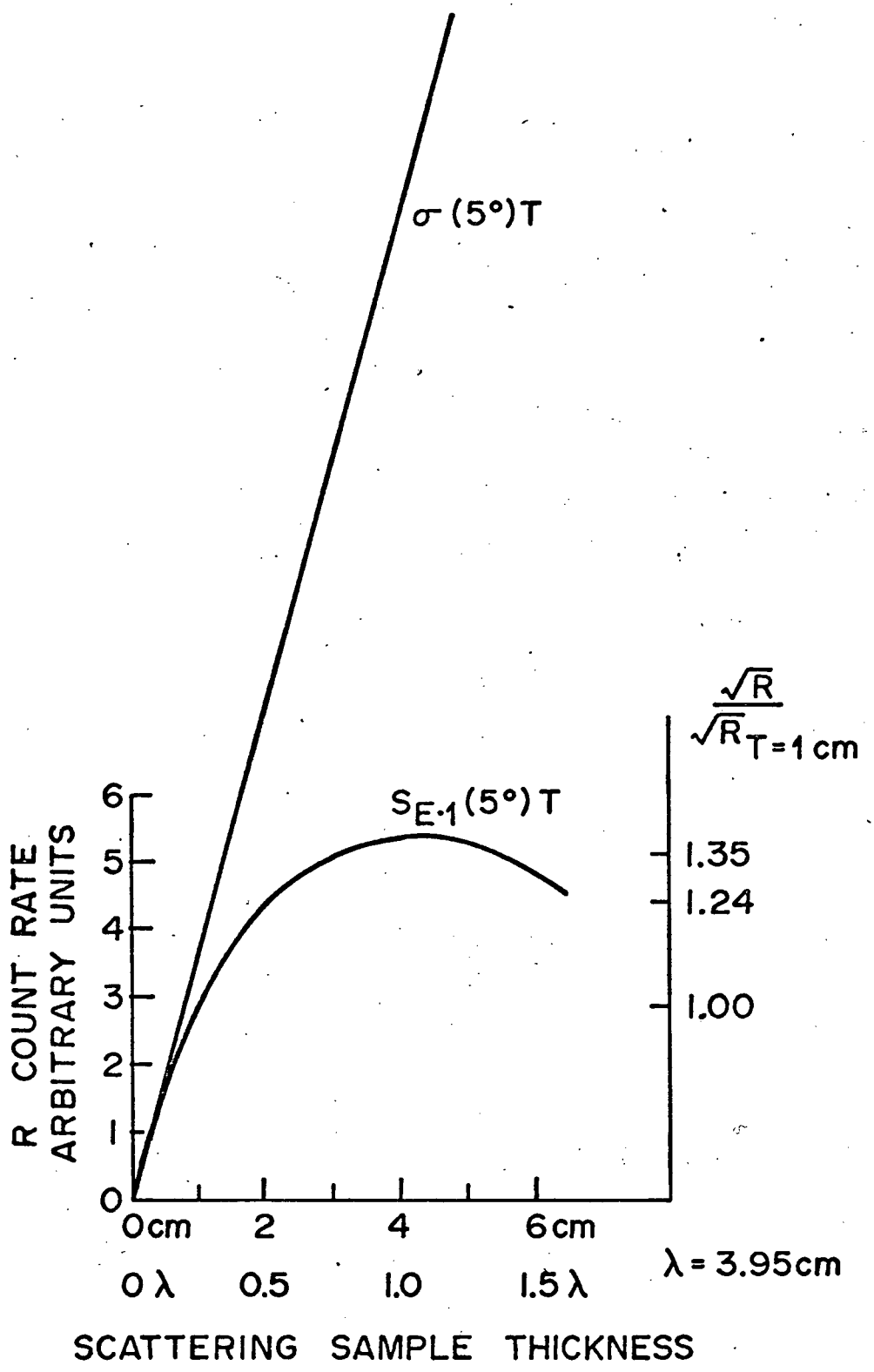

Figure A-2-8 Count Rate vs. Sample Thickness

(b) obtaining small neutron multiple scattering effects which are estimated with confidence.

The data obtained from the experiments described in the present work are interpreted as ratios of cross sections measured at 5^{o}, 10^{o} and 15^{o}. For t = 1 cm., the effects of multiple scattering on the ratio of cross sections over this angular range are shown in the table.

$\frac{S_{E\cdot 1}(5^{o})}{S_{E\cdot 1}(15^{o})}$	$\frac{S_{E\cdot 2}(5^{o})}{S_{E\cdot 2}(15^{o})}$	$\frac{S_{E\cdot 1}(5^{o})+S_{E\cdot 2}(5^{o})}{S_{E\cdot 1}(15^{o})+S_{E\cdot 2}(15^{o})}$	$\frac{\sigma\ (5^{o})}{\sigma\ (15^{o})}$
1.30	1.14	1.29	1.29

In order to test the analytical neutron multiple scattering formalism, data was taken for both t = 1 cm. and t = 2 cm. lead scattering samples. The angular distributions were integrated over angles for the two samples and the ratio, R_{expt} taken. This was compared with a similar ratio, R_{theo}, derived from the multiple scattering calculations.

$$R_{theo} = \frac{\sum_{\theta=5^{o},10^{o},15^{o}} (S_{E\cdot 1}(\theta) + S_{E\cdot 2}(\theta))_{t = 2\ cm.}}{\sum_{\theta=5^{o},10^{o},15^{o}} (S_{E\cdot 1}(\theta) + S_{E\cdot 2}(\theta))_{t = 1\ cm.}} = 0.822$$

$$R_{expt} = \frac{\sum_{\theta=5^{o},10^{o},15^{o}} (S_{E}(\theta)_{expt})_{t = 2\ cm.}}{\sum_{\theta=5^{o},10^{o},15^{o}} (S_{E}(\theta)_{expt})_{t = 1\ cm.}} = 0.848 \pm 5\%$$

The agreement is good and provides some experimental confirmation of the results of the calculation.

BIBLIOGRAPHY

Ad 69 A Adam et. al., Sov. J. Nucl. Phys. 8 (1969) 255.

Al 57 Y.A. Aleksandrov & I.I. Bondarenko, Sov. Phys. JETP 4 (1957) 612.

Al 58 Y.A. Aleksandrov, Sov. Phys. JETP 6 (1958) 228.

Al 61 Y.A. Aleksandrov et. al., Sov. Phys. JETP 13 (1961) 1319.

An 71 G.V. Anikin & I.I. Kotukhov, Sov. J. Nucl. Phys. 12 (1971) 614.

Au 62 E.H. Auerbach, Brookhaven Natl. Lab. Report, BNL 6562, 1962 (unpublished).

Au 64 E.H. Auerbach & S.O. Moore, Phys. Rev. 135 (1964) B895.

Ba 61 R. Batchelor et. al., Nucl. Inst. Meth. 13 (1961) 70.

Ba 65 R. Batchelor et. al., Nucl. Phys. 65 (1965) 236.

Bar 52 H.H. Barschall, Phys. Rev. 86 (1952) 431.

Bar 57 V.S. Barashenkov et. al., Sov. Phys. JETP 5 (1957) 144.

Bar 62 V.S. Barashenkov & H.J. Kaiser, Fortschr. Phys. 10 (1962) 33.

Bar 66 E. Barnard et. al., Nucl. Phys. 80 (1966) 46.

Bar 65 H.H. Barschall, Proceed. 2nd Internatl. Symp. Polarization Phenomena of Nucleons Karlsruhe 1965.

Bas 61 Proceed. Internatl. Symp. Polarization Phenomena of Nucleons Basel.
Helv. Phys. Acta, Suppl. VI (1961) 436.

Be 61 S. Bergia et. al., Phys. Rev. L. 6 (1961) 367.

Bo 54 N.A. Bostrom et. al., Texas Nuclear Corp. WADC-TN-59, 107 (1954).

Bo 69 A. Bohr & B. Mottleson, Nuclear Structure Vol. I page 183, W.A. Benjamin (1969).

Bo 63 P.H. Bowen et. al., Nucl. Phys. 40 (1963) 186.

Br 59 F.D. Brooks, Nucl. Inst. Meth. 4 (1959) 151.

Co 67 S.A. Cox, Nucl. Inst. Meth. 56 (1967) 245.

Dr 73 L. Drigo et. al., Nuovo Cimento 13 (1973) 867.

Du 61 P.S. Dubbledam & R.L. Walter, Nucl. Phys. 28 (1961) 414.

Du 63 Y.V. Dukarevich & A.N. Dyumin, Sov. Phys. JETP 17 (1963) 89.

El 64 A.J. Elwyn & J.E. Monahan, Argonne Natl. Lab. Report (1964).

El 66 A.J. Elwyn et. al., Phys. Rev. 142 (1966) 758.

Fe 54 H. Feshbach et. al., Phys. Rev. 96 (1954) 448.

Fo 69 G.C. Forrester, M.Sc. Thesis (1969), Univ. of British Columbia.

Ga 72 R.B. Galloway, Nucl. Inst. Meth. 105 (1972) 561.

Go 67 G.V. Gorlov et al., Sov. Phys. JETP 5 (1967) 106.

Go 67 G.V. Gorlov et. al., Phys. Lett. 25B (1967) 197.

Go 70 G.V. Gorlov et. al., Academy of Sciences USSR Bul., Physical Series, 34 (1970) 126.

Go 69 G.V. Gorlov et. al., Sov. J. Nucl. Phys. 8 (1969) 630.

Gr 67 T.B. Grandy, Ph.D. Thesis (1967) Univ. of Alberta.

Ha 52 J.A. Hauser & H. Feshbach Phys. Rev., 87 (1952) 366.

He 72 J.C.P. Heggie, Ph.D. Thesis (1972) Univ. of British Columbia.

Ho 63 P.E. Hodgson, The Optical Model of Elastic Scattering, Oxford Press, 1963.

Ho 67 P.E. Hodgson, Ann. Rev. Nucl. Sci. 17 (1967) 1.

Ho 69 W.S. Hogan & R.G. Seyler, Phys. Rev. 177 (1969) 1706.

Ig 70 S.I. Igarasi et. al., Nuclear Data for Reactors, Conf. Proceed., Helsinki 1970, Vol. II, page 869.

Ke 59 A.K. Kerman et. al., Ann. Phys. (N Y) 8 (1959) 551.

Ku 68 F.T. Kuchnir et. al., Phys. Rev., 176 (1968) 1405.

Ku 70 P. Kuijper et. al., Nucl. Inst. Meth. 77 (1970) 55.

Li 61 R.M. Littauer et. al., Phys. Rev. Let., 7 (1961) 141, 144.

McF 71 R.C. McFadden, P.W. Martin, & B.L. White, Nucl. Inst. Meth., 92 (1971) 563.

McF 73 R.C. McFadden & P.W. Martin, Nucl. Inst. Meth., 113 (1973) 601.

Ma 69 L.M. Makovsky & C. Hojvat, Nucl. Inst. Meth., 74 (1969) 342.

Ma 73 P.W. Martin, R.C. McFadden, & B.L. White, Can. J. Phys., 51 (1963) 2197.

Mi 52 Miller et. al., Phys. Rev., 85 (1952) 704.

Mi 52 Miller et. al., Phys. Rev., 88 (1952) 83.

Mo 64 J.E. Monahan & A.J. Elwyn, Phys. Rev., 136 (1964) B1678.

Mo 68 S.O. Moore, Brookhaven Natl. Lab. Report, BNL 50151 (1968).

Ok 59 P.L. Okhuysen & J.T. Prud'homme, Phys. Rev., 116 (1959) 986.

Pe 66 F. Pery, Nuclear Structure Study with Neutrons, Ed. M. Neve de Mevergnies et. al., 1966, page 418.

Re 65 R.F. Redmond, Internatl. Conf. on the Study of Nuclear Structure with Neutrons, Antwerp, 1965.

Re 66 W.B. Reid & R.H. Hummel, Can. Nucl. Tech., Jan.-Feb. 1966.

Ro 61 L. Rosen et. al., Phys. Rev. 124 (1961) 199.

St 65 L.G. Stronberg & S. Schwarz, Nucl. Phys. 71 (1965) 511.

St 73 C. Stassis, Phys. Rev., 7 (1973) 1926.

Th 63 D.B. Thompson, Phys. Rev. 129 (1963) 1649.

Tr 67 G.E. Tripard, Ph.D. Thesis, (1967) Univ. British Columbia.

Vo 69 E.W. Vogt, Proc. Int. Conf. "Properties of Nuclear States" Montreal 1969, Ed. M. Harvey et. al., page 5-33.

Wa 54 M. Walt & H.H. Barschall, Phys. Rev. 93 (1954) 1062.

Wa 55 M. Walt & J.R. Beyster, Phys. Rev., 98 (1955) 677.

Wa 64 M. Walt & D.B. Fossan, Phys. Rev., 137 (1965) B629.

Wi 64 D. Wilmore, UKAEC Rept., AERE-R4649, 1964.

Wo 56 L. Wolfenstein, Ann. Rev. Nucl. Sci., 6 (1956) 43.